# An Ultramicroporous Zinc-Based Zeolitic Imidazolate Framework-8 for the Adsorption of CO2 , CH4 , CO, N2 and H2 : A Combined Experimental and Theoretical Study

Sana Ahmed Khalil, Nadhem Missaoui, Raedah Alatawi, Ali Keshk, Obaidallah Alatawi, Tahani Albalawi, Andrew J. Gross

# An Ultramicroporous Zinc-based Zeolitic Imidazolate Framework-8 for the Adsorption of $CO_2$, $CH_4$, CO, $N_2$ and $H_2$: A Combined Experimental and Theoretical study

Sana Ahmed Khalil[1*], Nadhem Missaoui[2*], Raedah A. S. Alatawi[3], Ali A. Keshk[3], Obaidallah Alatawi[3], Tahani A. Albalawi[1], Andrew J Gross[4]

[1] Departement of Chemistry, Alwajh College, University of Tabuk, Tabuk, Saudi Arabia
[2] Laboratory of Interfaces and Advanced Materials, Faculty of Sciences, University of Monastir, Tunisia
[3] Departement of Chemistry, Faculty of Science, University of Tabuk, Tabuk 71474, Saudi Arabia
[4] Département de Chimie Moléculaire (DCM), Univ. Grenoble Alpes-CNRS, 570 rue de la chimie, 38041 Grenoble, France.

*Corresponding author: missaoui.nadhem1@gmail.com, sali@ut.edu.sa,

## Abstract

An alternative synthesis route to obtain ultramicroporous zeolitic imidazolate framework-8 (ZIF-8) is reported that is rapid and does not require organic solvent or heating. The polyethylene glycol-templated ZIF-8 nanoparticles (< 50 nm size) exhibited a high BET (Brunauer, Emmett and Teller) surface area of 1853 $m^2/g$, a total pore volume of 0.73 $cm^3/g$, and 0.54 nm ultramicropores. A new approach is introduced here to better understand gas adsorption in porous metal organic frameworks (MOFs) that combines theoretical and experimental isotherm data obtained for five gases with statistical physics modelling. The multiscale analytical model reveals that the gas molecules, irrespective of their structure, adsorb in a mixed orientation at low temperature, and a parallel multi-molecular orientation at higher temperature. The number of gas molecules adsorbed per site ranged from 0.83 to 2.2 while the number of adsorbent layers ranged between 1.4 to 5.6, depending on the gas and the temperature. The multilayer adsorption processes involved adsorption energies from 2.85 kJ/mol to 9.77 kJ/mol for all gases, consistent with physisorption *via* van der Waals and London dispersion forces. The initial adsorption energies were higher and therefore stronger. A particularly high capacity for $CO_2$ of 1088 mg($CO_2$)/g at 298 K was observed while $H_2$ adsorption was only 9 mg($H_2$)/g. The other gases adsorbed at 145 mg/g to 245 mg/g at 298 K. Thermodynamic functions that governed the adsorption process such as the internal energy, the enthalpy, and Gibbs free energy, are also reported, as well as the adsorption entropies, for the 5 gases.

## Introduction

Anthropogenic climate change is considered to be the single biggest threat facing humanity. Approximately 80% of all greenhouse gas emissions come from anthropogenic sources, including carbon dioxide ($CO_2$), one of the major greenhouse gases responsible for global

warming [1]. The amount of $CO_2$ in the atmosphere is considered to be around 400 ppm, which is 120 ppm more than during pre-industrial times [2]. To meet the temperature targets set forth in the Paris Agreement adopted in 2015, a significant decrease in global net greenhouse gas emissions as well as a shift towards "green" energy sources and technologies is necessary [3]. In the transportation sector, targets have been set for the use of clean renewable fuels like natural gas ($CH_4$) and hydrogen ($H_2$) as alternatives to conventional fossil fuels [4]. Largely due to their gaseous state at room temperature and non-condensable properties, $CO_2$, $CH_4$, or $H_2$ are difficult to store or capture [5-8]. It is also not trivial to separate gases such as $CO_2$ from these fuels. The challenges associated with hydrogen and methane adsorption predominantly revolve around the need for effective gas storage methods. The development of adsorbents for carbon dioxide on the other hand is driven largely by the need for effective capture and separation technologies to mitigate its emissions [9, 10]. One of the major challenges is achieving high level $CO_2$ adsorption and separation from flue gases, natural gas, $H_2$ gas, and air [10]. The adsorption and separation of CO and $N_2$ are essential for applications that include environmental protection, industrial processes, chemical synthesis, air separation, and workplace safety. The development of effective adsorption materials and separation processes for these gases is crucial towards improving health and safety, and product quality, and advancing sustainable practices [11].

Gas adsorption and separation are crucial processes for various industries, ranging from environmental protection to energy production [12-14]. Intricate engineering of efficient absorbents and membranes, as well as the development of effective separation techniques, is necessary to reduce greenhouse gas emissions and combat climate change. $CO_2$ can be effectively captured by chemical absorption methods such as those involving the use of dilute alkanol-amine solutions [15]. Solution-based methods offer simplicity and access to high absorption capacity, but solution regeneration has a high energy cost [16]. The corrosion and degradation of the reactive (e.g. the amine) component is also a problem [17, 18]. Porous adsorbents such as inorganic membranes [19], polymers [20], zeolites [21], and amino-functionalized nanocellulose aerogels [22] offer gas capture, separation and storage options based on physical adsorption processes. Such adsorbents nevertheless have limitations including unwanted reactivity, limited adsorption-desorption cycling stability, and limited gas selectivity and specificity. There is consequently significant interest in the development and understanding, ideally at the molecular level, of porous adsorbents with highly controlled pore and chemical structures for physical and/or chemical adsorption and separation of target species.

Metal organic frameworks (MOFs) which exhibit high surface areas and well-developed porosities with high tunability have emerged over the last two decades. MOF materials are attractive candidates for $CO_2$, $CH_4$, CO, $N_2$ and $H_2$ storage and/or separation. MOFs also offer commercialization potential due to their generally high thermal stability and low cost [23, 24]. The adsorption potential of MOFs is typically enhanced for MOFs comprising structures with micropore diameters of < 2 nm that correspond closely to the size of adsorbate molecules (the kinetic diameters of $H_2$, CO, $CO_2$, $N_2$ and $CH_4$ molecules are 0.29 nm, 0.30 nm, 0.33 nm, 0.36 nm and 0.38 nm, respectively) [25, 26]. As a subclass of MOFs, zeolitic imidazolate frameworks (ZIFs) with three-dimensional porous structures have demonstrated significant potential for gas adsorption and separation due to their large specific surface areas, variable pore diameters, including micropore and eventually ultramicropore structures [27-29], and outstanding chemical and thermal stabilities [30-32]. ZIFs are formed by coordination bonds between tetrahedral metal ($M^{2+}$) clusters and imidazolate linkers. ZIFs have proven to be particularly performant for the adsorption and separation of $CO_2$ and $CH_4$ [33-38]. In addition to their use for carbon dioxide capture and storage (CCS), ZIFs also have potential for the adsorption and/or storage of other gases such as $H_2$ [39-41].

ZIFs can be synthesized as microcrystals and/or nanocrystals using a wide range of methods to give unique porous materials with variable and tunable porosities and morphologies. Synthesis methods for ZIFs include solvothermal [42], ultrasonication [43], coordination-modulation [44], microwave-irradiation [45], microemulsion [46] and surfactant-assisted techniques [47]. ZIF-8 has a zeolite-like topology, classically comprising micropores, and exhibits excellent chemical and thermal stability, making it a highly versatile porous material for various applications [42, 48, 49]. ZIF-8 ($Zn(mIm)_2$ with mIm as 2-methylimidazolate)) has been prepared via various synthesis routes: solvothermal, sonochemical, dry-gel, microwave-assisted, mechanochemical, and microfluidic methods [42]. Han et al. reported a solvothermal synthesis method in N,N-diethylformamide (DEF) to obtain millimeter-scale single crystal ZIF-8 (SC-ZIF-8) using $HNO_3$ solution to control the initial nucleation rate [50].

Ultramicroporous nanocrystalline MOFs/or ZIFs such as PCN-13, Ni-Qc-5, ZU-36-Ni, Cu-F-pymo, $Fe(OH)(H_2bta)](H_2O)\}_n$ and ZIF-67 have been obtained in some cases [51-55]. The interest in MOF nanoparticles lies, for example, in the generally higher surface areas and larger number of accessible active sites [56]. Note: the term ‘microporous’ refers to porous materials or structures that have pores with diameters not exceeding 2 nm while the term ‘ultramicroporous’ refers to narrow micropores with approximate diameters of < 0.7 nm [57]. Ultramicropores

correspond more closely in size to certain gases and, for example, have proven to be especially effective for the selective adsorption and separation of molecules such as $CO_2$, $H_2$, and $CH_4$ with diameters ranging from ca. 0.25 to 0.7 nm [51-55].

We have recently developed the use of polyethylene glycol (PEG) as a sacrificial templating agent to modify the particle size and morphology of MOFs including ZIF-67 and ZIF-8 [29, 38]. This approach allows for the preparation of MOF particles with desirable properties such as ultramicroporosity and unusually high surface areas. PEG has previously been used during ZIF-8 synthesis for preparation of PEG-containing materials such as PEG/ZIF-8 polymer membranes [58], or PEG-modified ZIF-8 via coordination of the amino groups of PEG-$NH_2$ with $Zn^{2+}$ [59].

Sacrificial templating methods have been used to produce ZIF-8 in nano and/or microcrystalline forms including thin films and membranes, expanding their potential for gas separations, storage, catalysis, and sensing [60]. The use of PEG precursors to obtain ultramicroporous nanocrystalline ZIF-8 offers an exciting avenue for tailoring and optimizing MOF properties to meet specific requirements in gas separation and other advanced applications. ZIF-8 has a zeolite-like topology, classically comprising micropores, and exhibits excellent chemical and thermal stability, making it a highly versatile porous material for various applications [42, 48, 49, 61-66]. Nune et al. reported a synthesis method in methanol to obtain ultramicroporous ZIF-8 nanocrystals (n-ZIF-8) using 1% of high molecular weight poly(diallyldimethylammonium chloride) as a polymer template. The synthesis was performed at room temperature for 24 h and yielded a ZIF-8 adsorbent with a BET surface area of 1236 $m^2\ g^{-1}$, a micropore volume of 0.51 $cm^3g^{-1}$, and $CO_2$ adsorption capacity up to ~ 7.90 mmol ($CO_2$)/g (348 mg) at 298 K and 30 bar [67]. Yue et al. reported the synthesis of nanocrystalline ZIF-8 in methanol at ambient temperature but with a longer reaction time of 48 hours, achieving an adsorbent with BET surface area of 1264 $m^2\ g^{-1}$ [68]. We recently developed a synthesis method to obtain microporous ZIF-8 nanocrystals using a high molecular weight polyethylene glycol (PEG, $M_w$ = 20,000 g/mol) that also employed organic solvent but significantly shortened the reaction time to about 1 h. The PEG-templated ZIF-8 exhibited a maximum BET surface area of 1694 $m^2/g$ and a micropore volume of 0.67 $cm^3/g$, as well as attractive gas adsorption capacities for $CO_2$, $CH_4$ and $N_2$ of 547 mg ($CO_2$)/g, 211.58 mg ($CH_4$)/g and 136.37 mg ($N_2$)/g, respectively, at 298 K and 40 bar [38].

ZIF-8 nanoparticles with controlled dimensions and morphology can be manufactured utilizing a soft template such as a poly(diallyldimethylammonium chloride) polymer or

polyvinylpyrrolidone (PVP) polymer [67, 69]. Polymer-assisted synthesis plays a pivotal role in directing the nucleation and growth of ZIF-8 nanoparticles. By introducing polymers into the reaction mixture, it becomes possible to regulate the kinetics of crystal formation, resulting in a more controlled nucleation process. This controlled nucleation, in turn, may lead to the production of particles with more consistent sizes and shapes, ultimately yielding a higher degree of uniformity. For the first time, Kim et al. reported a surfactant-free, size-controllable, and scalable green synthesis method of ZIF-8 particles using four reaction parameters (temperature, concentration, pouring time, and reactant ratio) that affect the formation of nuclei and growth of ZIF-8 crystals [70]. The as-synthesized ZIF-8 nanoparticles show great uniformity and controllable particle sizes in the wide range of 147–915 nm. The classical solvothermal synthesis method (under the conditions: 140°C, 24 h, $Zn^{2+}$/mIm= 2/2 mmol) in DMF produced ZIF-8 with a BET surface area of 1370 $m^2/g$, 0.51 $cm^3/g$ for total pore volume and agglomerated particles, 0.5 to 1 μm in size [42]. These high temperature syntheses are beneficial for high crystallinity and gaining higher purity of the product, but one major disadvantage is that a long reaction times (for example, 24 h or even longer are needed for a quantitative yield of $Zn(mIm)_2$), the participation of a of the organic solvent and can be formed a by-product [42].

In recent years, numerous reports on the synthesis and evaluation of ZIF-8 samples for $CO_2$ capture have emerged (Table S1) [33, 35-37, 41, 67, 71-74]. For example, at 298 K temperature and 40 bar $CO_2$ pressure, ZIF-8 with a specific surface area ranging from 1264 to 1502 $m^2/g$ exhibited the capacity to adsorb $CO_2$ within the range of 347.6 to 469.9 mg($CO_2$)/g [67, 37, 73]. A direct correlation exists between the specific surface area of these ZIFs and their $CO_2$ uptake efficiency [67, 37, 73]. This phenomenon underscores the significance of maximizing the surface area in designing effective adsorbents for $CO_2$ capture. Researchers have dedicated considerable efforts to tailoring the structure of ZIFs to enhance their surface area and thus optimize their $CO_2$ adsorption capabilities. This insight has led to advancements in developing high-performance materials for addressing carbon dioxide emissions and climate-related challenges. The development of theoretical and analytical methods to better understand experimental adsorption data is key towards the development of new advanced porous MOF materials including microporous and ultramicroporous ZIFs. Most reported studies on the use of MOFs do not go far beyond the experimental observations, due to a lack of quantitative interpretations and modelling of physicochemical parameters. In several papers, conventional models have nevertheless been proposed for the phenomenological description of $CO_2$, $CH_4$, CO, $N_2$ and $H_2$ adsorption isotherms on ZIF-8 (e.g. Langmuir, Freundlich, Langmuir-Freundlich, Toth, Unilan, Sips, etc.)

[38, 41, 71, 73-76]. The fitting parameters contained in these classical models have only a mathematical meaning, and so only basic information can be deduced, such as the adsorption capacity at saturation and the adsorption energy that have a more empirical than physical meaning.

An important aim of this research study is to present a new theoretical approach to the modelling and analysis of $CO_2$, $CH_4$, CO, $N_2$ and $H_2$ adsorption at ultramicroporous MOFs via the application of advanced statistical physics to experimental data. Experimental adsorption isotherms were determined at temperatures between 273 K and 353 K and pressures from 0 to 40 bar to cover for diverse applications and operating environments, including those typically found in air and some flue gases [77]. Higher pressures were used to fully evaluate the temperature-dependent adsorption properties including under challenging or more extreme conditions. A statistical physics approach to interpret the experimental data is introduced using three advanced models to provide new understanding at the molecular level for the adsorption of $CO_2$, $CH_4$, CO, $N_2$ and $H_2$ at the ZIF-8 adsorbent. These advanced models were used for the first time for the description of $CO_2$, $CH_4$, CO, $N_2$ and $H_2$ adsorption at an ultramicroporous MOF. Physicochemical parameters such as the number of captured gas molecules per site, receptor site density, the number of formed layers, adsorbate orientation, and adsorption energies are reported, going beyond commonly used classical empirical models.

## Results and discussion

### Particle morphology of PEG-$_{400}$ templated ZIF-8 NPs

The morphology of PEG-$_{400}$ templated ZIF-8 NPs was examined by TEM (Figure S1 (a) and (b)). The TEM image reveals hexagonal particles with well-defined crystal surface structures that form agglomerations after drying [38, 78]. The well-defined crystalline structure of the synthesized PEG-$_{400}$ templated ZIF-8 NPs was further confirmed by the clearly visible edges and hexagonal facets. The particles had a Gaussian particle size distribution ranging from 10 to 50 nm with an average particle size of ~ 32 nm (Figure S1(c)), close to the size of the crystallites indicated by the XRD data and the Debye-Sherrer equation (see below).

Smaller nanoparticles as well as a narrower size distribution is reported here for the PEG-$_{400}$ templated ZIF-8 NPs (aqueous synthesis) compared to the PEG-$_{20.000}$ templated n-ZIF-8 (non-aqueous synthesis) that we recently reported [38]. For the PEG-$_{20.000}$ templated n-ZIF-8, a Gaussian size distribution from 60 to 260 nm (average particle size of ~ 150 nm) was reported [38]. Monomodal ZIF-8 particle sizes down to 30 nm have been obtained via synthesis in methanol

without a template [79]. The use of cetyltrimethylammonium bromide as a surfactant during aqueous ZIF-8 synthesis provided access to ca. 100 nm to 4 µm particle sizes [80]. The EDX elemental data shown in Figure S1 (d) demonstrates the expected elemental components of carbon (0.26 keV), nitrogen (0.53 keV) and zinc (1, 8.6, 9.8 keV), confirming the successful synthesis of well-defined PEG-$_{400}$ templated ZIF-8 NPs.

**XRD and FTIR characterization of PEG-400 templated ZIF-8 nanocrystals**

Powder X-ray diffraction patterns were recorded to investigate the crystallinity of the PEG-$_{400}$ templated ZIF-8 NPs, as shown in Figure. 1 (a). The characteristic diffraction peaks at 2θ values of 7.3°, 10.4°, 12.7°, 14.7°, 16.4°, 18° and 19.5°, 22.1°, 24.5°, 26.7° and 29.6° are assigned to ZIF-8: (011), (002), (112), (022), (013), (222), (114), (233), (134) and (044) planes, respectively. The peaks were compared with the experimental and simulated XRD data (CIF referenced CCDC 823083) reported by Cousin et al. [81].

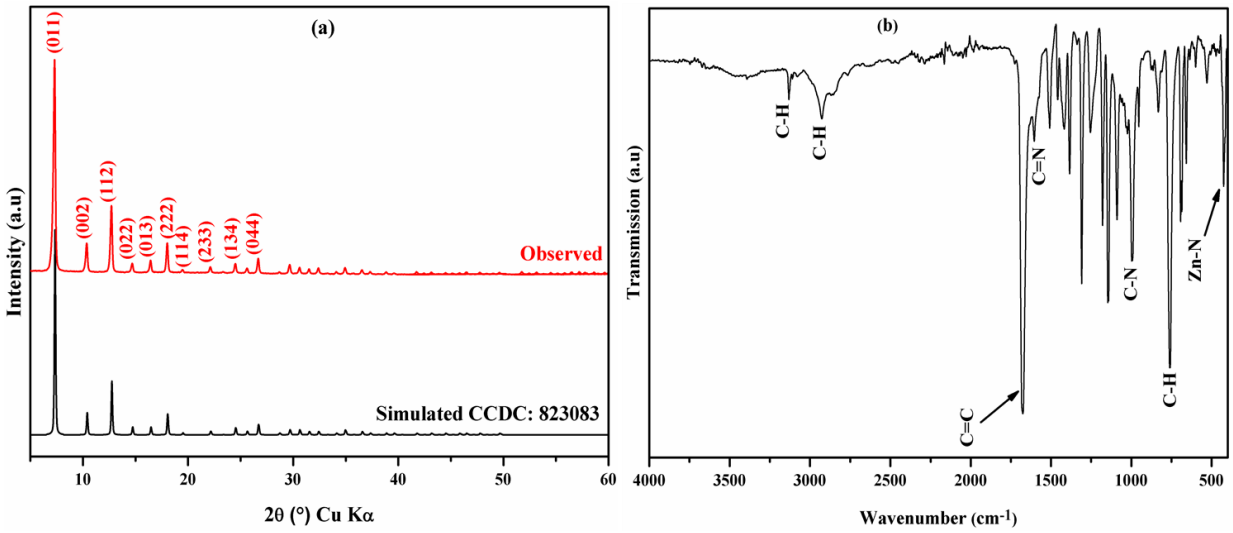


**Figure 1**. (a) XRD diffraction pattern of PEG-$_{400}$ templated ZIF-8 NPs: (black) simulated from the CIF reference: CCDC 671073; (red) as-prepared sample; (b) ATR-FTIR spectra of PEG-$_{400}$ templated ZIF-8 NPs.

The match between the experimental and simulated data confirms the high crystallinity of the PEG-templated ZIF-8 derivative prepared at room temperature without sonication or organic solvents. The data shows that no major impurities were detected at low or high 2θ. The peak at 2θ=7.3° (011) is used for crystallite size calculations in ZIF-8 XRD analysis. It is typically one of the most intense peaks in the XRD pattern. Using the Debye-Sherrer (equation (1)), the crystallite size was calculated as 49 nm, according to the following equation:

$$\Phi = \frac{K\lambda}{\beta cos\theta} \qquad \textbf{(1)}$$

Where **Φ** is the diameter of the crystallites (nm), $K$ is the numerical Scherrer constant (0.093 nm), $\lambda$ is the X-ray wavelength (0.154056 nm), $\beta$ is the full width at half-maximum intensity (FWHM) in radians, and $\theta$ is the Bragg diffraction angle.

The as-prepared PEG-$_{400}$ templated ZIF-8 NPs were subsequently studied using ATR-FTIR spectroscopy. The FTIR spectrum of n-ZIF-8 is shown in Figure 1 (b). The main bands at 3137, 2928, 1637, 1584, 1458, 1425, 1385, 1308, 1142, 995, 751, 694 and 424 $cm^{-1}$ are observed, consistent with spectra previously reported by Nadhem et al., Ordonez et al., Jomekian et al. and Cravillon et al. [38, 82-85]. Most bands correspond to the presence of methylimidazole ligands. The bands between 1500 and 600 $cm^{-1}$ may be attributed to the bending and stretching modes of the imidazole ring. The bands at 1142 and 1308 $cm^{-1}$ are assigned to the bending signals of the imidazole ring. The bands at 995 and 751 $cm^{-1}$ are associated with the bending vibrations of C–N and C–H, respectively. The band at 691 $cm^{-1}$ corresponds to the out-of-plane ring bending variation of the ligand. The band at 1637 $cm^{-1}$ is due to the C=C stretching mode, while the band at 1584 $cm^{-1}$ is ascribed to the stretching mode of C=N. The weak bands at 2928 and 3137 $cm^{-1}$ are associated with the asymmetric stretching mode of aliphatic C–H. Importantly, the Zn–N stretching vibration band at 424 $cm^{-1}$ is clearly observed, consistent with the chemical combination of Zn(II) ions with the nitrogen of the methylimidazole ligands, and the resulting formation of imidazolate bonds.

**TGA and specific surface area analysis of PEG-400 templated ZIF-8 NPs**

The thermal stability is an important characteristic for high temperature application of porous adsorbent materials. The thermal stability of PEG-$_{400}$ templated ZIF-8 NPs was evaluated by TGA from 300 K to 1200 K (Figure S2 (a)). As the sample was heated it underwent two weight loss stages. A small ca. 2 % weight loss is first observed in the temperature range of 300-500 K, attributed to the removal of guest molecules such as water or gas molecules (e.g., $H_2O$, $CO_2$). A significant weight loss of ca. 62-64% occurred as the temperature was increased from 660 to 800 K, corresponding to significant thermal decomposition of ZIF-8 NPs. The PEG-$_{400}$ templated ZIF-8 NPs exhibit higher thermal stability compared to previously reported ZIF-8 materials [78, 86]. After the TGA experiment was completed, we performed further characterization experiments on the degradation product. Zinc oxide (ZnO) was identified by XRD as the final calcination product of PEG-$_{400}$ templated ZIF-8 NPs after treatment up to ca. 1150 K (Figure S2 (b)). The peaks and corresponding diffraction angles are perfectly matched with the ZnO nanoparticles pattern (JCPDS card No: 75-1526) [87]. Overall, these results show that the synthesized PEG-$_{400}$

templated ZIF-8 NPs exhibits good thermal stability up to 700 K, which is appropriate for numerous applications. The size, volume and surface area of the pores are crucial parameters that substantially affect the gas adsorption properties of porous materials. The porous properties of the PEG-templated n-ZIF-8 NPs were examined based on nitrogen adsorption/desorption isotherms measured at 77 K (Figure 2 (a)). The adsorbent exhibits rapid $N_2$ uptake at low relative pressure ($10^{-5}$< P/P° <$10^{-2}$). The behaviour corresponds to a typical type I isotherm according to the IUPAC classification, confirming the microporosity of the material [38, 88]. The $N_2$ adsorption/desorption isotherms for the PEG-$_{400}$ templated ZIF-8 NPs are completely reversible and reproducible, consistent with a stable and rigid material having a permanent structural porosity. A BET surface area ($S_{BET}$) of 1853 $m^2/g$ was determined from the data collected at 0.05 < P/P° < 0.35 for the PEG-$_{400}$ templated ZIF-8 NPs. The surface area is significantly greater compared to PEG-$_{20.000}$ templated n-ZIF-8 prepared via synthesis in N,N–dimethylformamide (1694 $m^2/g$) [38], and surpasses most imidazolate-based ZIFs (595-1502 $m^2/g$) (Table S1) [33, 35-37, 67, 71, 73]. The aqueous PEG-templated synthesis with the shorter chain PEG-$_{400}$ is clearly advantageous compared to the non-aqueous synthesis with the much larger PEG-$_{20.000}$ in terms of achieving smaller NPs with a narrower size distribution and significantly greater surface area. The total pore volume ($V_{micro}$) of 0.73 $cm^3/g$ determined at P/P° = 0.99 is comparable to the 0.67 $cm^3/g$ for the PEG-$_{20.000}$ templated n-ZIF-8 [38]. Figure 2 (b) highlights the presence of two pore size distributions located at 0.54 nm (ultramicropores) and 0.89 nm (micropores). The introduction and strong influence of ultramicropores in the ZIF-8 structure has been shown to favor the adsorption of $CO_2$ (0.33 nm) over $N_2$ (0.364 nm) and $CH_4$ (0.38 nm) molecules [89].

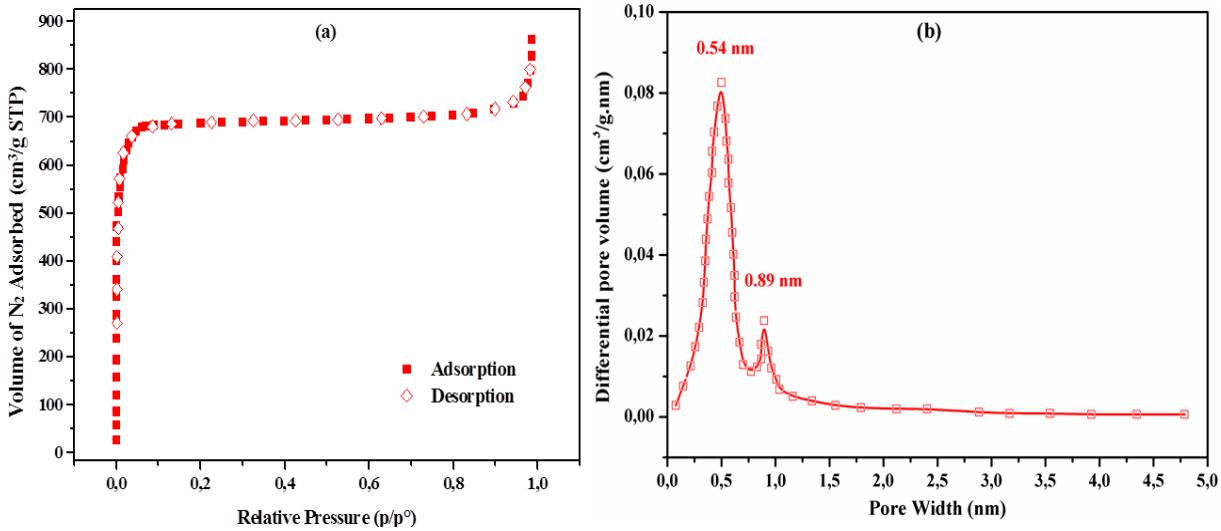


**Figure 2.** (a) $N_2$ adsorption/desorption isotherms obtained at 77 K and (b) corresponding pore size distribution for PEG-templated ZIF-8 NPs.

**Gas adsorption study with $CO_2$, $CH_4$, $N_2$, $H_2$ and CO**

Adsorption isotherms were recorded for five gases at various temperatures (273, 298, 323, and 353 K) and pressures (0-40 bar) (Figure S3). Generally, the adsorption of $CO_2$, $CH_4$ and CO increased with elevated pressure until the uptake reached saturation (type I behavior). The adsorption of $N_2$ and $H_2$ increased linearly or quasi-linearly with increasing pressure. The $CO_2$ adsorption capacity was considerably higher compared to the other gases and followed the general trend: $CO_2$ >>> $CH_4$ > CO > $N_2$ >> $H_2$ for a given temperature and pressure. The PEG-$_{400}$ templated ZIF-8 NPs displayed better adsorption capacities for $CO_2$, $CH_4$ and $N_2$ compared to the recently reported high performing PEG-$_{20.000}$ templated n-ZIF-8 [38]. The adsorption capacity of PEG-$_{400}$ templated ZIF-8 at 298 K and 40 bar $CO_2$ was 1088.21 mg($CO_2$)/g. To our knowledge, this is the maximum $CO_2$ adsorption capacity reported for a ZIF-8 adsorbent (see Table S1). This exceptional capacity can be associated with the amalgamation of the small sub-100 nm particle size and narrow size distribution, large BET surface area, and the important contribution of introduced ultramicropores. Under the same conditions, the adsorption capacity for $CH_4$ was 244.58 mg($CH_4$)/g, while the CO, $N_2$ and $H_2$ adsorption capacities were 172.52 mg(CO)/g, 145.46 mg($N_2$)/g and 9.24 mg($H_2$)/g, respectively. For PEG-$_{20.000}$ templated n-ZIF-8, the gas adsorption capacities under the same condition (298 K and 40 bar) were 547 mg($CO_2$)/g, 211.58 mg($CH_4$)/g and 136.37 mg($N_2$)/g, corresponding to increases in adsorption capacity by 98%, 16% and 7%, respectively [38]. The adsorption improvement for $CO_2$ is especially noteworthy, further highlighting the importance of the pore structure and surface area, including the small nanoparticle size and narrow size distribution. For all pressures in the 1-40 bar range, the adsorption capacities for all 5 gases ($CO_2$, $CH_4$, CO, $N_2$, $H_2$) increased with decreasing temperature.

The small sizes of $CO_2$ and $N_2$ of ca. 0.33 and 0.36 nm, respectively, correspond well with the 0.54 nm ultramicropores. The larger quadrupole moment of $13.4\times10^{-40}$ C.m$^2$ for $CO_2$ ($4.7\times10^{-40}$ C.m$^2$ for $N_2$) may also support the superior interaction of $CO_2$ via physisorption at the surface of n-ZIF-8 [90, 91]. These factors do not however account for the adsorption behavior of $CH_4$ since $CH_4$ has no quadrupole moment (nonpolar molecule) [92]. $CO_2$, $N_2$ and $CH_4$ also possess differences in their electronic properties and therefore polarizability. The higher $CH_4$ adsorption capacity compared to $N_2$ can be linked to its greater polarizability ($17.6\times10^{-25}$ vs. $26.0\times10^{-25}$ cm$^3$ for $N_2$ and $CH_4$, respectively) [93].

The experimentally-obtained adsorption isotherms for $N_2$, $H_2$, CO, $CO_2$, and $CH_4$ at PEG-$_{400}$ templated ZIF-8 NPs (Figure S3) were subsequently used to implement the statistical physics

approach (Equation (2)). The adsorption isotherm data after fitting with the multilayer model with saturation (MMS) is shown in Figure 3.

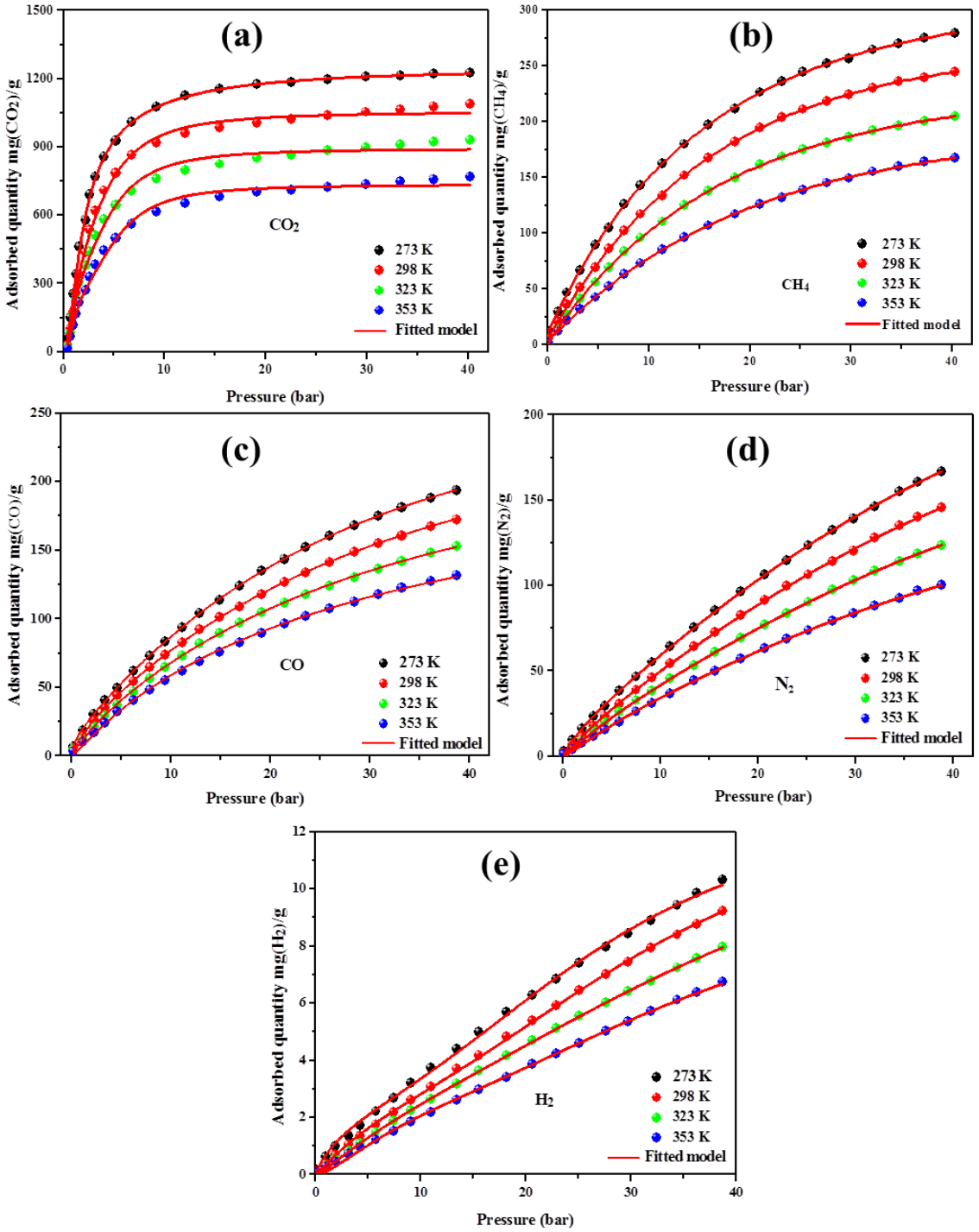


**Figure 3.** Experimental isotherm with corresponding lines of best fit according to the multilayer model with saturation (MMS model) for (a) $CO_2$, (b) $CH_4$, (c) CO, (d) $N_2$ and (e) $H_2$ at PEG-400 templated ZIF-8 NPs at different temperature (273, 298, 323 and 353 K) and high pressure (0-40 bar).

An analytical model of statistical physics (AMSP) was used to fit the data to obtain a better understanding of the interactions between different gaseous molecules and the n-ZIF-8 nanoparticles. Importantly, this approach allowed the extraction of parameters such as adsorption energies. The multilayer model assumes the formation of a number of layers ($N_2$) of gas molecules on the surface of PEG-$_{400}$ templated ZIF-8 NPs *i.e.* that the surface of the adsorbent reaches saturation at elevated gas pressures. The interactions between the first layer of gas molecules and the adsorption sites are characterized by the first adsorption energy $(-\varepsilon_1)$. The adsorption of secondary and further layers is characterized by the second adsorption energy $(-\varepsilon_2)$. The equilibrium adsorbed quantity as a function of pressure, associated to this model, is given by the following relation (equation (2)) [94-101]:

$$Q_{eq}=\left(n_{gm}\times D_{as}\right)\times\left(\frac{-2.\left(\frac{P}{P_1}\right)^{(2.n_{gm})}}{1-\left(\frac{P}{P_1}\right)^{n_{gm}}}+\frac{\left(\frac{P}{P_1}\right)^{n_{gm}}\times\left(1-\left(\frac{P}{P_1}\right)^{(2.n_{gm})}\right)}{\left(1-\left(\frac{P}{P_1}\right)^{n_{gm}}\right)^2}+\frac{2.\left(\frac{P}{P_1}\right)^{n_{gm}}\times\left(\frac{P}{P_2}\right)^{n_{gm}}\times\left(1-\left(\frac{P}{P_2}\right)^{(n_{gm}.N_2)}\right)}{\left(1-\left(\frac{P}{P_2}\right)^{n_{gm}}\right)}-\frac{N_2\times\left(\frac{P}{P_1}\right)^{n_{gm}}\times\left(\frac{P}{P_2}\right)^{n_{gm}}\times\left(\frac{P}{P_2}\right)^{(n_{gm}.N_2)}}{\left(1-\left(\frac{P}{P_2}\right)^{n_{gm}}\right)}+\frac{\left(\frac{P}{P_1}\right)^{n_{gm}}\times\left(\frac{P}{P_2}\right)^{(2.n_{gm})}\times\left(1-\left(\frac{P}{P_2}\right)^{(n_{gm}.N_2)}\right)}{\left(1-\left(\frac{P}{P_2}\right)^{n_{gm}}\right)^2}}{\frac{\left(1-\left(\frac{P}{P_1}\right)^{(2.n_{gm})}\right)}{\left(1-\left(\frac{P}{P_1}\right)^{n_{gm}}\right)}+\frac{\left(\frac{P}{P_1}\right)^{n_{gm}}\times\left(\frac{P}{P_2}\right)^{n_{gm}}\times\left(1-\left(\frac{P}{P_2}\right)^{(n_{gm}.N_2)}\right)}{\left(1-\left(\frac{P}{P_2}\right)^{n_{gm}}\right)}}\right)$$

**(2)**

Where $n_{gm}$ is the number of gaseous molecules ($H_2$, $N_2$, CO, $CO_2$ and $CH_4$) that are captured per adsorption site, $D_{as}$ is the gas density, $P_1$ and $P_2$ are the pressures at half saturation, and $N_{TL}$ $(1+N_2)$ is the total number of layers of gaseous molecules formed on the surface of the adsorbent surface. Compared to conventional adsorption models, this statistical physics model can unravel information such as the orientation of adsorbed gaseous molecules on the PEG-$_{400}$ templated ZIF-8 NPs surface and the effective global number of adsorbate layers at different operating temperatures. Note: multivariable nonlinear regression utilizing the Levenberg Marquardt procedure was used to fit the data in Figure 3. The calculated parameters based on the advanced model are given in Table 1.

**Table 1.** Physicochemical parameters predicted by the AMSP Multilayer Model with Saturation (MMS) via least squares regression fitting of experimentally-determined gas adsorption isotherm data using Origin software.

| T(K) | $R^2$ | $n_{gm}$ | $D_{as}$ (mg/g) | $N_2$ | $P_1$ (bar) | $P_2$ (bar) | $Q_{sat}$ (mg/g) |
|---|---|---|---|---|---|---|---|
| | | | | **$N_2$** | | | |
| **273** | 0.999 | 0.81±0.032 | 98.38±0.31 | 2.92±0.012 | 12.91±0.04 | 44.46±0.072 | 312.37±0.32 |
| **298** | 0.999 | 1.03±0.042 | 68.53±0.132 | 2.63±0.052 | 10.23±0.012 | 42.63±0.081 | 256.22±0.72 |
| **323** | 0.999 | 1.08±0.043 | 56.42±0.435 | 2.56±0.013 | 10.28±0.043 | 42.83±0.082 | 216.92±0.83 |
| **353** | 0.999 | 1.18±0.034 | 41.36±0.130 | 2.38±0.022 | 9.36±0.036 | 40.03±0.073 | 164.96±0.62 |
| | | | | **$H_2$** | | | |
| **273** | 0.998 | 0.90±0.01 | 2.87±0.01 | 4.57±0.031 | 3.46±0.025 | 28.79±0.023 | 14.38±0.023 |
| **298** | 0.999 | 1.13±0.03 | 2.66±0.02 | 3.68±0.020 | 6.04±0.042 | 33.51±0.032 | 14.06±0.032 |
| **323** | 0.999 | 1.23±0.02 | 2.91±0.03 | 2.86±0.034 | 9.30±0.037 | 41.64±0.033 | 13.81±0.018 |
| **353** | 0.998 | 1.56±0.04 | 1.81±0.04 | 2.65±0.047 | 7.67±0.031 | 36.74±0.036 | 10.30±0.052 |
| | | | | **CO** | | | |
| **273** | 0.999 | 0.55±0.011 | 134.80±0.32 | 3.21±0.032 | 16.30±0.032 | 27.90±0.032 | 312.12±0.32 |
| **298** | 0.999 | 0.81±0.012 | 112.06±0.38 | 2.14±0.032 | 9.76±0.071 | 37.75±0.038 | 285.01±0.37 |
| **323** | 0.999 | 0.97±0.03 | 86.96±0.33 | 1.88±0.032 | 8.26±0.052 | 38.95±0.072 | 242.93±0.38 |
| **353** | 0.998 | 1.20±0.06 | 67.88±0.38 | 1.50±0.032 | 8.06±0.035 | 42.35±0.038 | 203.64±0.88 |
| | | | | **$CO_2$** | | | |
| **273** | 0.999 | 1.83±0.03 | 480.64±0.770 | 0.41±0.022 | 1.66±0.033 | 6.74±0.038 | 1240.19±0.037 |
| **298** | 0.995 | 1.97±0.05 | 239.90±0.322 | 1.23±0.032 | 1.22±0.037 | 4.63±0.033 | 1053.90±0.044 |
| **323** | 0.992 | 2.09±0.06 | 179.75±0.432 | 1.38±0.012 | 1.09±0.022 | 4.86±0.052 | 894.11±0.025 |
| **353** | 0.993 | 2.15±0.07 | 133.79±0.327 | 1.56±0.013 | 1.13±0.012 | 5.36±0.042 | 736.38±0.033 |
| | | | | **$CH_4$** | | | |
| **273** | 0.998 | 0.88±0.031 | 227.99±0.038 | 0.97±0.038 | 10.06±0.052 | 26.21±0.022 | 395.24±0.32 |
| **298** | 0.999 | 0.95±0.033 | 85.08±0.033 | 2.66±0.04 | 3.54±0.031 | 17.70±0.041 | 298.82±0.41 |
| **323** | 0.999 | 0.98±0.032 | 65.81±0.032 | 2.76±0.032 | 3.41±0.037 | 17.64±0.033 | 242.49±0.44 |
| **353** | 0.998 | 1.29±0.040 | 37.70±0.037 | 2.87±0.034 | 2.31±0.037 | 18.04±0.071 | 188.20±0.51 |

**Assessment of steric parameters during gas adsorption**

**Number of gaseous molecules captured per adsorption site ($n_{gm}$)**

The parameter $n_{gm}$ provides valuable information concerning the adsorption of gas molecules at the PEG-$_{400}$ templated ZIF-8 NPs. Notably; this parameter allows one to identify the adsorption orientation as well as the accumulation behavior of the gaseous molecules at the nanoparticle surface. There are three possibilities that can be envisaged according to the $n_{gm}$ value [94-96]:

- If $n_{gm} < 0.5$, the adsorption site is considered to capture a fragment of one molecule per site, leading to a parallel adsorption orientation and therefore a multi-interaction adsorption mechanism.
- If $0.5 < n_{gm} < 1$, it is considered that the $N_2$, $H_2$, CO, $CO_2$ and $CH_4$ molecules are accommodated in a non-parallel and parallel orientation with two different degrees, simultaneously.

- If $n_{gm} \geq 1$, the active adsorption site takes up one or more gaseous molecules, and the adsorption position is non-parallel, indicating a multi-molecular adsorption phenomenon.

The values of $n_{gm}$ at low temperature for all given gaseous molecules, except for $CO_2$, are between 0.50 and 1 (Table 1). This reveals that $H_2$, $N_2$, CO, $CO_2$ and $CH_4$ single molecules or fragments adsorb via a mixed adsorption orientation (i.e., non-parallel and parallel simultaneously) at low temperatures. The $n_{gm}$ values for $CO_2$ at low temperatures of 273 K and 298 K are vastly greater at 1.83 and 1.97 compared to the other gases, highlighting a different interaction mechanism for $CO_2$ under these conditions. More specifically, the data is consistent with multi-molecular adsorption for $CO_2$ at single adsorption sites vs. more partial or single molecular adsorption for the other gases at low and ambient temperature. In other words, multi-molecular adsorption of $CO_2$ in non-parallel orientation is strongly favored at ultramicroporous ZIF-8, even when gas molecules possess less kinetic energy and diffusional mobility. At elevated temperatures, the number of molecules captured per adsorption site is greater than unity, suggesting that the adsorption process becomes multi-molecular, and that each site can captures several gas molecules. The impact of temperature on the number of gaseous molecules captured per adsorption site is represented in Figure 4. We note that gas adsorption was less effective for all gases at higher temperature (Figure 3) hence the multi-molecular mechanism does not generally correlate to higher adsorption capacity.

The number of adsorbed gaseous molecules per site increased with temperature for all given gases: from 0.81 to 1.18, from 0.90 to 1.56, from 0.55 to 1.20, from 1.83 to 2.15 and from 0.88 to 1.29, respectively, for $N_2$, $H_2$, CO, $CO_2$, and $CH_4$. Consequently, it can be inferred that the adsorption systems are thermally activated, and that the temperature has a favorable influence (i.e., enhancement in $n_{gm}$) on the aggregation (or accumulation) of gaseous molecules, and especially so for the smaller CO (0.30 nm) and $H_2$ molecules (0.29 nm). This change in adsorption mechanism is related to the kinetic energy of the gas molecules and the probability of non-parallel collisions at the surface, and/or the thermodynamics of the process. The accumulation behavior during adsorption is clearly not simply related to steric effects, even if the smaller size of $CO_2$ is considered beneficial for physical gas adsorption compared to other gases.

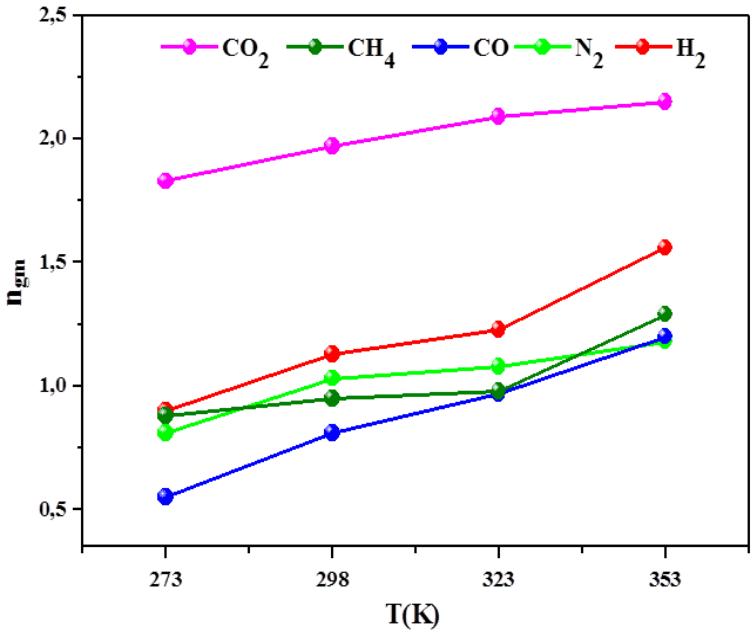


**Figure 4.** Effect of temperature on the number of gaseous molecules captured per adsorption site ($n_{gm}$) for $N_2$, $H_2$, CO, $CO_2$, and $CH_4$ on PEG-$_{400}$ templated ZIF-8 NPs.

**Density of adsorption sites ($D_{as}$)**

The influence of temperature on the density of adsorption sites, $D_{as}$, was considered and is plotted in Figure 5. This parameter reflects the density per surface unit of active receptor sites. The plot shows that higher temperatures from 273 K to 353 K induced a decline in the density of receiver sites for all of the gases at the PEG-$_{400}$ templated ZIF-8. This is in contrast to the data obtained for the $n_{gm}$ parameter where the number of molecules per adsorption site increased with temperature. The decrease in the density of adsorption sites coincides with an increasing affinity for multi-layer adsorption of gas molecules at single sites via non-parallel adsorption. Both the $D_{as}$ and $n_{gm}$ appear to be strongly impacted by thermal agitation effects that in turn affect molecular interactions with the adsorbent. The rise in temperature is believed to trigger the blockage of certain pores or functional groups at the surface of the adsorbent that would otherwise be used to bond gas molecules. The formation of static aggregates that inhibit or block active sites at the surface may also be considered.

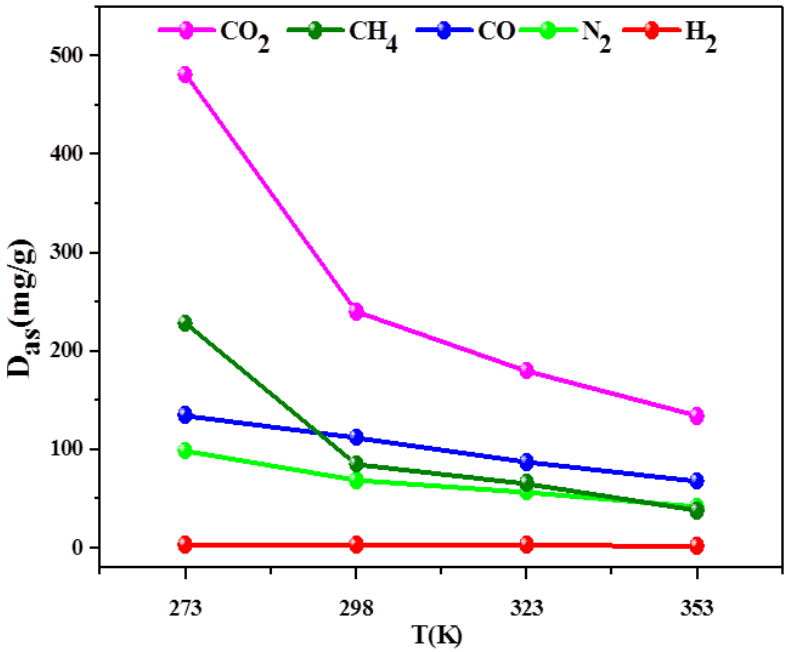


**Figure 5.** Effect of temperature on the density of adsorption sites ($D_{as}$) for $N_2$, $H_2$, CO, $CO_2$, and $CH_4$ on PEG-$_{400}$ templated ZIF-8 NPs.

**Total number of adsorbed layers ($N_{TL}$)**

The parameter $N_{TL} = 1+N_2$ allows us to identify the total number of formed layers during the adsorption process. The relationship between temperature and the global number of formed layers ($N_{TL}$) is reported in Figure 6.

The data obtained using the statistical physics model demonstrates that the total number of layers formed ranged from 3.92 to 3.38, 5.57 to 3.65, 4.21 to 2.50, 1.41 to 2.56, and 1.97 to 3.87 for $N_2$, $H_2$, CO, $CO_2$ and $CH_4$, respectively (Figure 6). This analysis reveals that the adsorption process at the surface of the adsorbent involves the creation of between 1 and 6 layers, depending on the type of molecule and the temperature. For example, for the case of $N_2$, the number of molecules (expressed in percentage) for the 3.92 multilayers that adsorb at the adsorbent surface at 273 K can be approximated using the following relationship: $N_{TL} = 3\times y + (1-y)\times 4$ where y is the percentage of $N_2$ molecules that entered via three layers and (1-y) addresses the adsorbed molecules associated to four layers, respectively. Accordingly, it was considered that 92% of $N_2$ molecules were adsorbed on the PEG-$_{400}$ templated ZIF-8 NPs surface, creating four layers, and that the remaining 8% of the gas molecules corresponded to three layers.

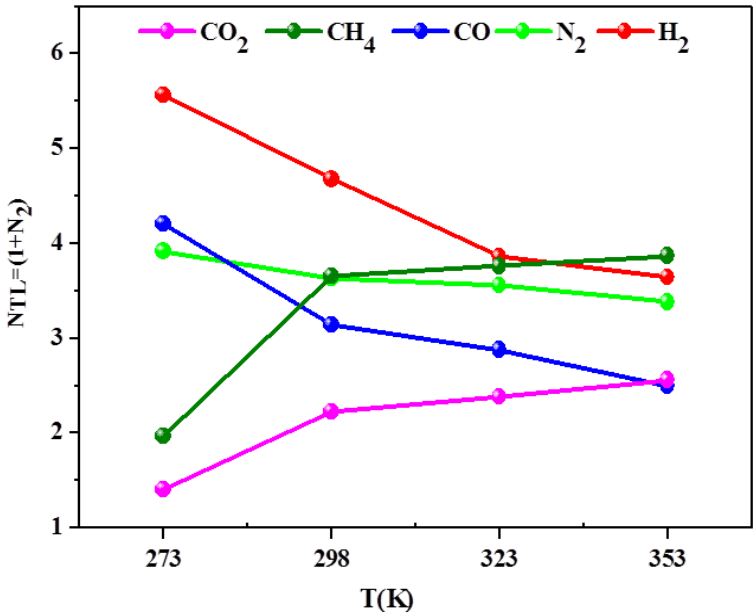


**Figure 6.** Effect of temperature on the total number of adsorbed layers ($N_{TL}$) for $N_2$, $H_2$, CO, $CO_2$, and $CH_4$ on PEG-$_{400}$ templated ZIF-8 NPs.

From a thermal viewpoint, the total number of layers of $N_2$, $H_2$ and CO gaseous molecules formed on the adsorption sites diminished as a function of temperature. This reduction can be correlated to classical effects of thermal agitation; for example, increased desorption that leads to a reduction in the number of adsorbed layers. In contrast, for $CO_2$ and $CH_4$ molecules, the total number of layers increased with increasing temperature, which might be related to the different interaction energies of these gas molecules with the adsorbent. The different trend for $CO_2$ and $CH_4$, which show the highest adsorption capacities, appears to highlight the presence of specific and unique adsorbate-adsorbent interactions that favor for the adsorption of multiple layers as the temperature increases. It's important to note that the highest adsorption capacities observed for $CO_2$ and $CH_4$ were obtained when 1-2 layers. In contrast, the best adsorption capacities for the gases which adsorbed much less efficiently were obtained when 4-6 layers of gas adsorbed.

**Adsorption quantity at saturation ($Q_s$)**

The capability of the PEG-$_{400}$ templated ZIF-8 NPs to capture $N_2$, $H_2$, CO, $CO_2$ and $CH_4$ molecules is represented by the adsorption capacity at saturation ($Q_s$). This parameter, determined from the MMS model, is depicted as the maximum amount of gas that may be adsorbed at a given temperature.

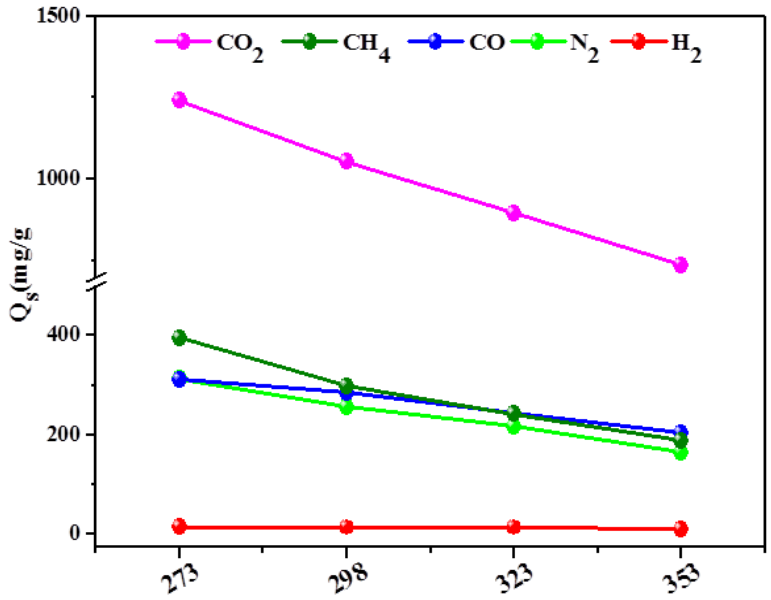


**Figure 7.** Effect of temperature on the adsorption capacity at saturation ($Q_s$) based on the MMS model for $N_2$, $H_2$, CO, $CO_2$ and $CH_4$ molecules on PEG-$_{400}$ templated ZIF-8 NPs.

Figure 7 shows the impact of temperature on the adsorption capacity at saturation for the different gases. The adsorption capacity at saturation declines with increasing temperature, reflecting the exothermic character of the process (e.g. release of heat that favours adsorption at lower temperature). This behaviour is consistent with a weakening in binding strength between the adsorbent and adsorbate for all 5 gas molecules as the temperature increases. This trend of decreasing saturation adsorption capacity may be connected to the other determined parameters including the various steric parameters ($n_{gm}$, $D_{as,}$ and $N_L$) and kinetics of gas adsorption.

**Analysis of the surface adsorption energies**

To further unravel the adsorption process, we retrieved parameters relating to the energetic intensity of the adsorbate-adsorbent interactions. The adsorption energies for $N_2$, $H_2$, CO, $CO_2$ and $CH_4$ molecules bound at the PEG-$_{400}$ templated ZIF-8 NPs surface were determined using the multilayer model with saturation (MMS). In particular, referring to the MMS equation, the two pressures at half saturation (i.e., $P_{ls1}$ and $P_{ls2}$) were used to determine the two adsorption energies ($-\Delta E^a{}_1$) and ($-\Delta E^a{}_2$), according to the following expressions (equation (3) and (4)), which in turn allow investigation of their relationship with temperature [94, 102-107]:

$$-\Delta E^a{}_1 = -R.T.\ln(\frac{P_{vs}}{P_{ls1}}) \quad \textbf{(3)}$$

$$-\Delta E^a{}_2 = -R.T.\ln(\frac{P_{vs}}{P_{ls2}}) \quad \textbf{(4)}$$

Where $P_{vs}$ is the saturated vapor pressure of the gas at the corresponding temperature and R is the gas constant ($8.314x10^{-3}$ kJ.K$^{-1}$.mol$^{-1}$). Above the critical temperature ($T_c$) for $N_2$, $H_2$, CO and $CH_4$, Dubinin (1975) proposed the following empirical expression for calculating the pseudo-vapor pressure values (equation (5)).

$$P_{vs} = P_c \left( \frac{T}{T_c} \right)^2 \qquad \textbf{(5)}$$

Where $P_c$ represents the $CO_2$ critical pressure.

**Table 2.** Estimated energies for the adsorption of $CH_4$, $CO_2$, CO, $N_2$ and $H_2$ at PEG-$_{400}$ templated ZIF-8 NPs.

| **$CH_4$** | $\Delta E^a_1$ **(kJ/mol)** | $\Delta E^a_2$ **(kJ/mol)** |
|---|---|---|
| T=273 K | 5.068±0.031 | 2.894±0.012 |
| T=298 K | 8.554±0.022 | 4.566±0.013 |
| T=323 K | 9.804±0.032 | 5.397±0.022 |
| T=353 K | 12.380±0.031 | 6.347±0.072 |
| **$CO_2$** | $\Delta E^a_1$ **(kJ/mol)** | $\Delta E^a_2$ **(kJ/mol)** |
| T=273 K | 8.095±0.037 | 4.915±0.033 |
| T=298 K | 10.034±0.031 | 6.730±0.033 |
| T=323 K | 11.611±0.036 | 7.597±0.034 |
| T=353 K | 13.105±0.032 | 8.536±0.037 |
| **CO** | $\Delta E^a_1$ **(kJ/mol)** | $\Delta E^a_2$ **(kJ/mol)** |
| T=273 K | 4.993±0.071 | 3.773±0.021 |
| T=298 K | 7.156±0.051 | 3.804±0.033 |
| T=323 K | 8.637±0.052 | 4.472±0.041 |
| T=353 K | 10.032±0.033 | 5.163±0.042 |
| **$H_2$** | $\Delta E^a_1$ **(kJ/mol)** | $\Delta E^a_2$ **(kJ/mol)** |
| T=273 K | 12.440±0.030 | 7.631±0.012 |
| T=298 K | 12.633±0.031 | 8.388±0.015 |
| T=323 K | 12.967±0.032 | 8.941±0.017 |
| T=353 K | 15.258±0.041 | 10.660±0.022 |
| **$N_2$** | $\Delta E^a_1$ **(kJ/mol)** | $\Delta E^a_2$ **(kJ/mol)** |
| T=273 K | 5.664±0.032 | 2.857±0.078 |
| T=298 K | 7.193±0.011 | 3.657±0.078 |
| T=323 K | 8.216±0.016 | 4.384±0.078 |
| T=353 K | 9.776±0.018 | 5.511±0.032 |

Table 2 shows the adsorption energies determined via the MSS model with equations (3) and (4). It is noted that the first adsorption energy ($-\Delta E^{a}_{1}$) is related to the relationship between the gas molecules and the active site of the PEG-$_{400}$ templated ZIF-8 NPs adsorbent surface. The second adsorption energy ($-\Delta E^{a}_{2}$) concerns the interaction involving successive layers of gas molecules at the adsorbent surface. For all temperatures, the gas molecules adsorbed in successive layers exhibited the weakest interactions i.e. $\Delta E^{a}_{2}$ energies ranging from 2.85 kJ/mol to 5.55 kJ/mol. Stronger interaction energies were determined for the first adsorption layer and consistently increased with increasing temperature (with $\Delta E^{a}_{1}$ energies ranging from 5.66 kJ/mol to 9.77 kJ/mol). $CO_2$ exhibits strong adsorption energies compared to the other gases, except for $H_2$ which exhibited the highest adsorption energies for all conditions. High adsorption energy does not correlate with a high capacity for adsorption; in fact, the highest energies were observed when the adsorption capacities were the smallest. Several factors may contribute to this trend, such as the limited availability of adsorption sites and the formation of multilayers. The adsorption energies predicted using the model were all found to be less than 30 kJ/mol, consistent with physisorption via interactions such as van der Waals and London dispersion forces. Additionally, all adsorption energies were negative, further supporting the exothermic nature of $CH_4$, $CO_2$, CO, $N_2$ and $H_2$ adsorption at PEG-$_{400}$ templated ZIF-8 NPs.

**Thermodynamic functions**

The MMS model was subsequently used to evaluate the thermodynamics of adsorption for the five gases; namely, $CH_4$, $CO_2$, CO, $N_2$ and $H_2$, at PEG-$_{400}$ templated ZIF-8 NPs. The thermodynamic potentials provide information about the equilibrium proprieties and the mechanical, energetical and morphological transformations that take place [94, 84, 103-110]. Following earlier microscopic studies of adsorption processes at different materials [103-110], here we perform a macroscopic study via calculation of the different thermodynamic potentials such as: the internal energy, $E_{int}$, and the Gibbs free enthalpy, $G_a$, of the system [103-110]. We used the chosen model expression, or more precisely, the partition function of the adsorption system, to follow the evolution of adsorbate-adsorbent interactions at the equilibrium state that relates to the thermodynamic state under the experimental conditions. The expressions of these variables were determined using the canonical and grand canonical ensembles of statistical physics formalism, as detailed in the following section.

**The total internal energy for the adsorbate-adsorbent system**

The thermodynamic investigation of a system starts with its internal energy, E. In our case, we focused specifically on the interaction between the adsorbate and the surface of the adsorbent [94, 98, 103-110]. The internal energy represents all forms of energy in the total system. It represents the adsorption energy due to the interaction between the adsorbate molecules and the adsorbent surface. For our adsorbate-adsorbent system, the $CH_4$, $CO_2$, CO, $N_2$ or $H_2$ gas molecules are considered to move in a gaseous phase. The internal energy of free adsorbate molecules is therefore given by equation (6): [103-110]:

$$E_{\text{int}} = -\frac{\partial \ln(Z_{gc})}{\partial \beta} + \frac{\mu}{\beta}\left(\frac{\partial \ln(Z_{gc})}{\partial \mu}\right) \qquad \textbf{(6)}$$

The internal energy, $E_{int}/k_BT$, has the following expression (equation (7)):

$$\frac{E_{aint}}{k_B T} = D_{as} \times \left\{ \ln\left(\frac{P}{z_v}\right) \frac{\left(\frac{P}{P_1}\right)^{n_{gm}} + \left(2.\left(\frac{P}{P_1}\right)^{n_{gm}} \times \left(\frac{P}{P_2}\right)^{n_{gm}}\right).\frac{\left(1-\left(\frac{P}{P_2}\right)^{n_{gm} N_2}\right)}{\left(1-\left(\frac{P}{P_2}\right)^{n_{gm}}\right)} + \left(\left(\frac{P}{P_1}\right)^{n_{gm}} \times \left(\frac{P}{P_2}\right)^{n_{gm}}\right).\frac{\left(\frac{P}{P_2}\right)^{n_{gm}} \times \left(\left(1-\left(\frac{P}{P_2}\right)^{n_{gm} N_2}\right) - N_2\left(\frac{P}{P_2}\right)^{n_{gm} N_2}\left(1-\left(\frac{P}{P_2}\right)^{n_{gm}}\right)\right)}{\left(1-\left(\frac{P}{P_2}\right)^{n_{gm}}\right)^2}}{\left(1+\left(\frac{P}{P_1}\right)^{n_{gm}}\right) + \left(\left(\frac{P}{P_1}\right)^{n_{gm}}\left(\frac{P}{P_2}\right)^{n_{gm}}\right) \times \frac{\left(1-\left(\frac{P}{P_2}\right)^{n_{gm} N_2}\right)}{\left(1-\left(\frac{P}{P_2}\right)^{n_{gm}}\right)}} - \right.$$

$$\left. \frac{\left(\left(\frac{P}{P_1}\right)^{n_{gm}} \times \ln\left(\frac{P}{P_1}\right)^{n_{gm}}\right) + \left(\left(\frac{P}{P_1}\right)^{n_{gm}} \times \ln\left(\frac{P}{P_1}\right)^{n_{gm}} \times \left(\frac{P}{P_2}\right)^{n_{gm}} \times \ln\left(\frac{P}{P_2}\right)^{n_{gm}}\right) \times \frac{\left(1-\left(\frac{P}{P_2}\right)^{n_{gm} N_2}\right)}{\left(1-\left(\frac{P}{P_2}\right)^{n_{gm}}\right)} + \left(\left(\frac{P}{P_1}\right)^{n_{gm}} \times \left(\frac{P}{P_2}\right)^{2n_{gm}}\right) \times \frac{\ln\left(\frac{P}{P_2}\right)^{n_{gm}} \times \left(1-\left(\frac{P}{P_2}\right)^{n_{gm} \cdot N_2}\right) - N_2 \times \left(\ln\left(\frac{P}{P_2}\right)^{n_{gm}} \times \left(\frac{P}{P_2}\right)^{n_{gm} \cdot N_2}\right) \times \left(1-\left(\frac{P}{P_2}\right)^{n_{gm}}\right)}{\left(1-\left(\frac{C}{C_2}\right)^{n_{gm}}\right)^2}}{\left(1+\left(\frac{P}{P_1}\right)^{n_{gm}}\right) + \left(\left(\frac{P}{P_1}\right)^{n_{gm}} \times \left(\frac{P}{P_2}\right)^{n_{gm}}\right) \frac{\left(1-\left(\frac{P}{P_2}\right)^{n_{gm} \cdot N_2}\right)}{\left(1-\left(\frac{P}{P_2}\right)^{n_{gm}}\right)}} \right\}$$

**(7)**

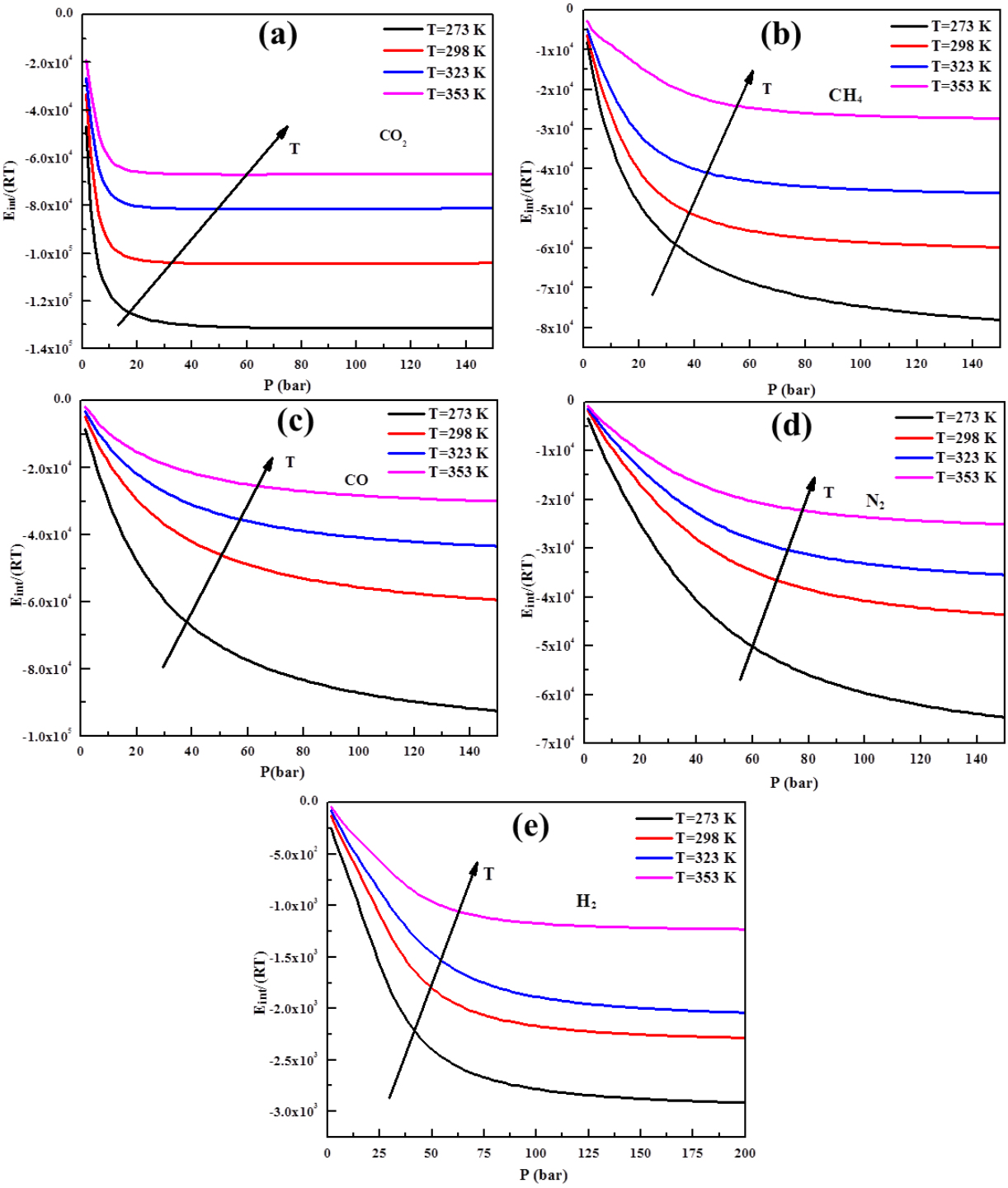


**Figure 8.** Variation of internal energy as a function of equilibrium pressure for (a) $CO_2$, (b) $CH_4$, (c) CO, (d) $N_2$ and (e) $H_2$ at PEG-$_{400}$ templated ZIF-8 NPs.

Figure 8 shows the variation in the $E_{int}$ values (adsorption internal energy) for $CH_4$, $CO_2$, CO, $N_2$ and $H_2$ at PEG-templated n-ZIF-8 as a function of temperature. All of the determined internal energies values were found to be negative, highlighting that the adsorption system liberates energy as a spontaneous process. The decrease in internal energies corresponds to the amount of work available to introduce the $CH_4$, $CO_2$, CO, $N_2$ and $H_2$ molecules being increased on the PEG-

templated n-ZIF-8 as a function of temperature. Therefore, the adsorption process involving $CH_4$, $CO_2$, CO, $N_2$ and $H_2$ and the adsorbent are exothermic in nature.

**Adsorption enthalpy ($H_a$)**

The adsorption enthalpy ($H_a$) is a vital parameter for understanding the thermodynamic aspects of adsorption processes. Generally, the enthalpy change signifies the amount of heat that is either added, or the work done, during the adsorption process [94, 98, 103-110]. It provides insights into the heat exchange characteristics of a specific transformation process. This thermodynamic potential can be expressed through the following relationship:

$$H_a = U + PV = G + TS \quad \textbf{(8)}$$

$$dH = TdS - VdP \quad \textbf{(9)}$$

Where P represents the pressure, V is involved as the gas volume, U is equal to the internal energy ($U = E_{int}$), G is the Gibbs free enthalpy of adsorption, and S is the configurational entropy. The evolution of the determined adsorption enthalpy versus the pressure of gas molecules is plotted in Figure 9. Firstly, the data in Figure 9 shows that the adsorption enthalpies are negative and therefore exothermic, regardless of the pressure and gas. The enthalpies do not surpass 80 kJ/mol. This observation is consistent with the adsorbate-adsorbent bonding interaction being predominantly of the hydrogen bond type and/or van der Waals type interactions [105-108]. As the pressure increases, there is a corresponding decrease in enthalpy. This suggests that both the heat and work can be transferred to the system in an arbitrary manner. In our specific case, the decreases in enthalpy represent the amount of available work that is being transformed into heat generated by the adsorption reaction.

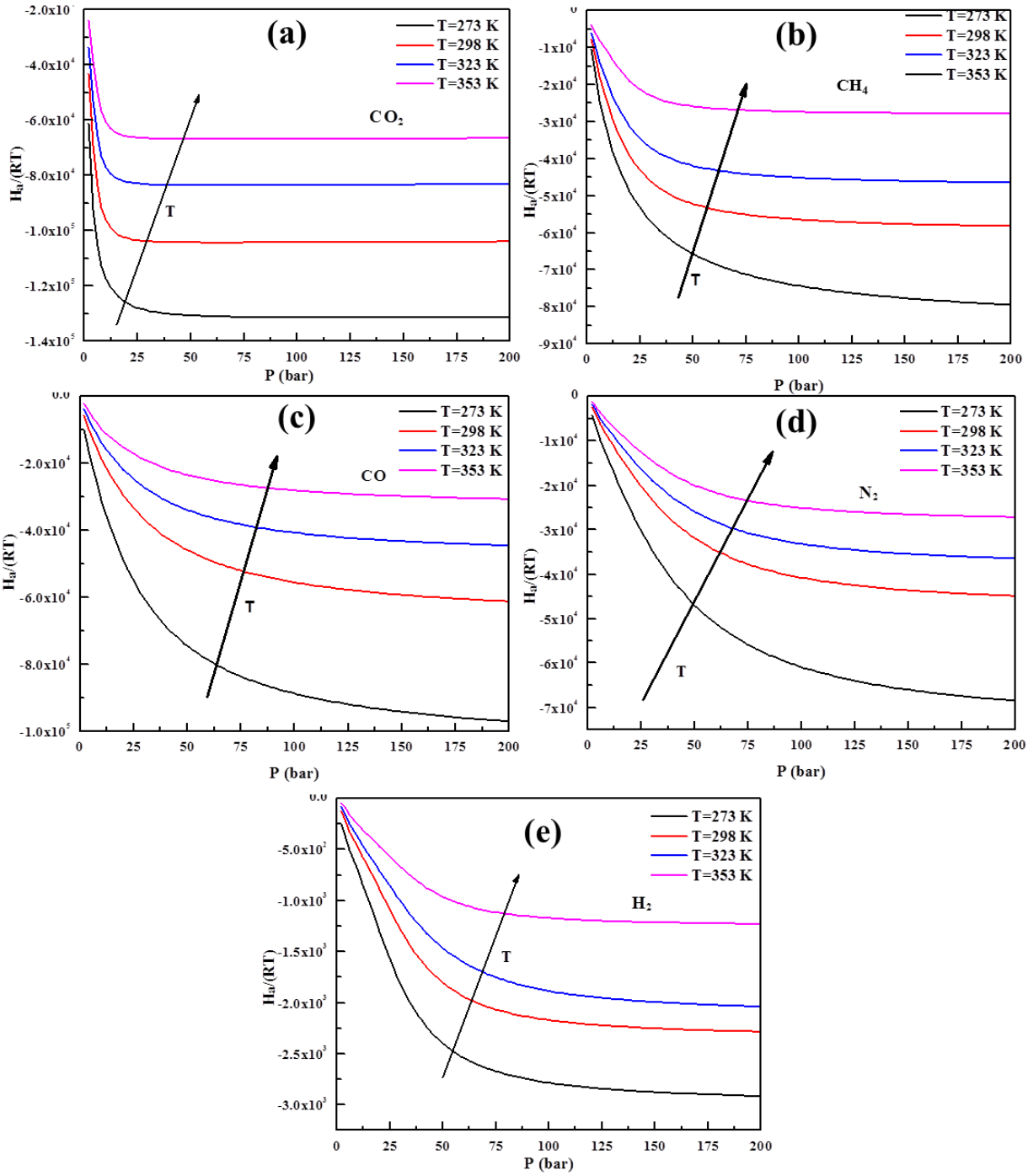


**Figure 9.** Variation of adsorption enthalpy as a function of equilibrium pressure at different temperatures for (a) $CO_2$, (b) $CH_4$, (c) CO, (d) $N_2$ and (e) $H_2$ at PEG-$_{400}$ templated ZIF-8 NPs.

### The entropy of adsorption ($S_a$)

The entropy information plays a critical role in characterizing the behavior of adsorbed molecules. It quantifies the mobility of gas molecules (such as $N_2$, $H_2$, CO, $CO_2$, and $CH_4$) in relation to the receptor sites on the surface of PEG-$_{400}$ templated ZIF-8 NPs. In the realm of statistical thermodynamics, adsorption entropy is defined as a thermodynamic function that

measures the disorder of the system at a microscopic level. The overall system consists of adsorbate molecules that are in contact with the adsorbent surface. The expression for the entropy of adsorption ($S_a$) can be written as follows (equation (10)):

$$\frac{S_a}{k_B} = Ln(Z_{gc}) - \beta \frac{\partial Ln(Z_{gc})}{\partial \beta} \qquad \textbf{(10)}$$

By utilizing the expression of the grand canonical function, $Z_{gc}$, for the monolayer model, we can derive the equation for the adsorption entropy [96, 99]. Subsequently, the overall adsorption entropy, $S_a$, of the system can be determined by employing the following equation (11):

$$\frac{S_a}{k_B} = D_{as} \times \ln\left(1+\left(\frac{P}{P_1}\right)^{n_{gm}}+\left(\frac{P}{P_1}\right)^{n_{gm}}\times\left(\frac{P}{P_2}\right)^{n_{gm}}\times\left(\frac{\left(1-\left(\frac{P}{P_2}\right)^{n_{gm}\cdot N_2}\right)}{\left(1-\left(\frac{P}{P_2}\right)^{n_{gm}}\right)}\right)\right) - \frac{\left(\ln\left(\frac{P}{P_1}\right)^{n_{gm}}\times\left(\frac{P}{P_1}\right)^{n_{gm}}+\left(\frac{P}{P_1}\right)^{n_{gm}}\times\left(\frac{P}{P_2}\right)^{n_{gm}}\times\ln\left(\frac{P}{P_1}\right)^{n_{gm}}\times\ln\left(\frac{P}{P_2}\right)^{n_{gm}}\times\left(\frac{\left(1-\left(\frac{P}{P_2}\right)^{n_{gm}\cdot N_2}\right)}{\left(1-\left(\frac{P}{P_2}\right)^{n_{gm}}\right)}\right)+\left(\frac{P}{P_1}\right)^{n_{gm}}\times\left(\frac{P}{P_2}\right)^{n_{gm}}\times\left(\frac{\ln\left(\frac{P}{P_2}\right)^{n_{gm}}\times\left(\frac{P}{P_2}\right)^{n_{gm}}\times\left(1-\left(\frac{P}{P_2}\right)^{n_{gm}\cdot N_2}\right)-N_2\times\ln\left(\frac{P}{P_2}\right)^{n_{gm}}\times\left(\frac{P}{P_2}\right)^{n_{gm}}\times\left(\frac{P}{P_2}\right)^{n_{gm}\cdot N_2}\times\left(1-\left(\frac{P}{P_2}\right)^{n_{gm}}\right)}{\left(1-\left(\frac{P}{P_2}\right)^{n_{gm}}\right)^2}\right)\right)}{\left(1+\left(\frac{P}{P_1}\right)^{n_{gm}}+\left(\frac{P}{P_1}\right)^{n_{gm}}\times\left(\frac{P}{P_2}\right)^{n_{gm}}\times\left(\frac{\left(1-\left(\frac{P}{P_2}\right)^{n_{gm}\cdot N_2}\right)}{\left(1-\left(\frac{P}{P_2}\right)^{n_{gm}}\right)}\right)\right)}$$

**(11)**

Consideration of the entropy provides information about the level of disorder and randomness exhibited by the gas molecules during the adsorption process. Figure 10 illustrates the variation of entropy with pressure at different temperatures for the 5 gases at PEG-$_{400}$ templated ZIF-8 NPs. At low pressures, the entropy increases, indicating a higher degree of disorder during gas adsorption. This can be attributed to improved availability of numerous receptor sites for gas adsorption. At high pressures, a reduction in entropy and therefore disorder is observed. This reduction occurs due to a decrease in the number of available free sites. At higher pressures, all five gas molecule types have a lower probability of finding an unoccupied receptor site. This occurs as the adsorbent approaches saturation and tends to exhibit a more ordered arrangement.

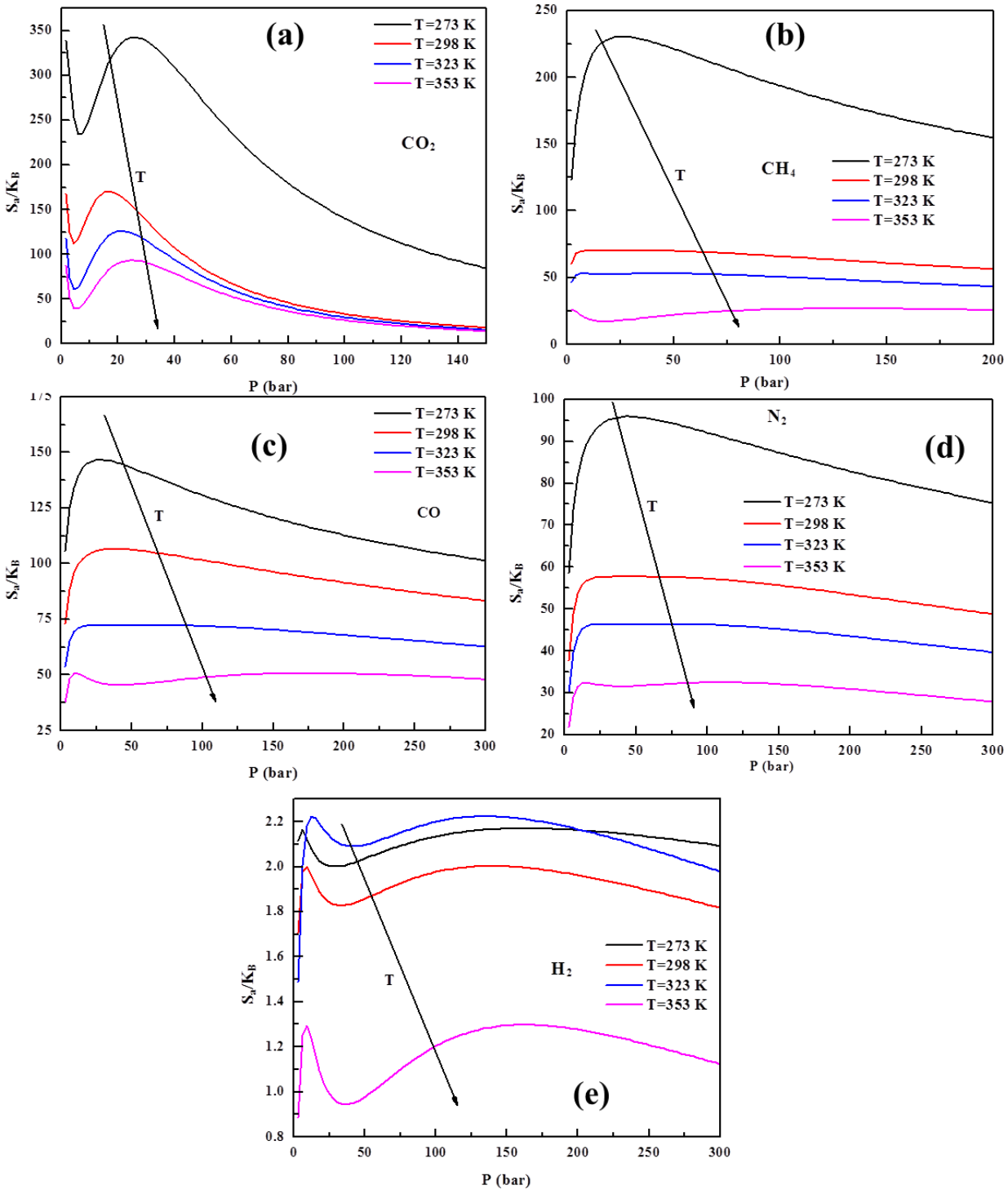


**Figure 10.** Variation of adsorption entropy as a function of equilibrium pressure at different temperatures for (a) $CO_2$, (b) $CH_4$, (c) CO, (d) $N_2$ and (e) $H_2$ at PEG-$_{400}$ templated ZIF-8 NPs.

### Gibbs free enthalpy of adsorption (G) for the adsorbate-adsorbent

The Gibbs free enthalpy is a thermodynamic function of the system that depends on the behavior of the external environment. The Gibbs free enthalpy of adsorption, G, is a thermodynamic potential function that gives information about the spontaneity of the adsorption process [103-110].

A spontaneous process of adsorption is characterized by G function values that evolve to lower values and therefore a more thermodynamically stable energy state [94, 98]. The evolution of a spontaneous system can consequently be studied by using the variation of the Gibbs free enthalpy, ΔG. This function allows us to define the orientation of the reaction adsorption process and its position at equilibrium. If ΔG < 0, the system develops as a spontaneous process and tends to an equilibrium state. If ΔG = 0, the system is at equilibrium. The Gibbs free enthalpy is defined by the following expression (equation (12)): [111-113].

$$G = H - TS = E + PV - TS \qquad \textbf{(12)}$$

Where G is the exchanged energy due to the variation of particle adsorption spontaneity of gas molecules on the adsorbent surface. We can determine the expression for the Gibbs free enthalpy of adsorption, G, of our system, according to the following equation (13):

$$\frac{G_a}{(k_B T)} = n_{gm} \times D_{as} \times \ln\left(\frac{\beta.P}{z_v}\right) \times \frac{\dfrac{\left(-2.\left(\dfrac{P}{P_1}\right)^{2n_{gm}}\right)}{\left(1-\left(\dfrac{P}{P_1}\right)^{n_{gm}}\right)} + \dfrac{\left(\dfrac{P}{P_1}\right)^{n_{gm}} . \left(1-\left(\dfrac{P}{P_1}\right)^{2n_{gm}}\right)}{\left(1-\left(\dfrac{P}{P_1}\right)^{n_{gm}}\right)^2} + \dfrac{2\left(\dfrac{P}{P_1}\right)^{n_{gm}} . \left(\dfrac{P}{P_2}\right)^{n_{gm}} . \left(1-\left(\dfrac{P}{P_2}\right)^{n_{gm}N_2}\right)}{\left(1-\left(\dfrac{P}{P_2}\right)^{n_{gm}}\right)} + \dfrac{N_2\left(\dfrac{P}{P_1}\right)^{n_{gm}}\left(\dfrac{P}{P_2}\right)^{n_{gm}}\left(\dfrac{P}{P_2}\right)^{n_{gm}N_2}}{\left(1-\left(\dfrac{P}{P_2}\right)^{n_{gm}}\right)} + \dfrac{\left(\dfrac{P}{P_1}\right)^{n_{gm}}\left(\dfrac{P}{P_2}\right)^{2n_{gm}}\left(1-\left(\dfrac{P}{P_2}\right)^{n_{gm}N_2}\right)}{\left(1-\left(\dfrac{P}{P_2}\right)^{n_{gm}}\right)^2}}{\dfrac{\left(1-\left(\dfrac{P}{P_1}\right)^{2n_{gm}}\right)}{\left(1-\left(\dfrac{P}{P_1}\right)^{n_{gm}}\right)} + \dfrac{\left(\dfrac{P}{P_1}\right)^{n_{gm}}\left(\dfrac{P}{P_2}\right)^{n_{gm}}\left(1-\left(\dfrac{P}{P_2}\right)^{n_{gm}N_2}\right)}{\left(1-\left(\dfrac{P}{P_2}\right)^{n_{gm}}\right)}}$$

**(13)**

Figure S4 shows the variation in the estimated Gibbs free energy values as a function of pressure for the different temperatures for $N_2$, $H_2$, CO, $CO_2$, and $CH_4$. The Gibbs free energy, $G_a$, was negative, which further validates the spontaneous nature of the adsorption reaction. This thermodynamic function also decreased with increasing temperature, consistent with a strong effect of thermal agitation that decreases the spontaneity of the adsorption process at higher temperatures for the PEG-$_{400}$ templated ZIF-8 NPs adsorbent.

## Conclusions

In summary, polyethylene glycol (PEG-$_{400}$)-templated crystalline n-ZIF-8 nanoparticles with a well-defined size distribution have been successfully synthesized in entirely aqueous conditions without the need for organic solvent. The room temperature synthesis method is convenient and

rapid (≤ 5 min) and provides access to small and narrowly distributed n-ZIF-8 particles of < 50 nm size. The nanoparticles possess a very high BET surface area of 1853 $m^2\ g^{-1}$, thanks in part to the presence of ultramicropores. Experimental adsorption isotherm data is reported at four different temperatures (273 K to 353 K) for $CO_2$, $CH_4$ and $N_2$, as well as for $N_2$ and $H_2$ gases. The adsorbent showed very high adsorption performance for $CO_2$ i.e. 1088 mg ($CO_2$)/g at room temperature. A statistical multi-layer physics model with saturation was applied to the experimental data to extract various parameters such as the number of gaseous molecules per site ($n_{gm}$), the receptor site density ($D_{as}$), and energetic parameters ($-\Delta E^a_1$) and ($-\Delta E^a_2$). Thermodynamic functions such as the entropy, the Gibbs free energy, the adsorption enthalpy and the internal energy, were also evaluated. The determined values provide new insight relating to the number of layers of adsorbates to the orientation of molecules and the stability of the adsorption processes at different temperatures. While significant differences in adsorption are reported, the gaseous adsorption for all five gases clearly shows that the adsorption process on n-ZIF-8 is spontaneous, exothermic, multilayer, and physical in nature. The adsorption enthalpy data reveals that the adsorption processes for n-ZIF-8 is exothermic, resulting in the release of heat to the outside. The application of the statistical physics model to other metal organic frameworks and molecular adsorbents promises to allow improved understanding of the gas adsorption processes of these new highly porous materials.

## Experimental

### Materials

Zinc nitrate hexahydrate ($Zn(NO_3)\cdot 6H_2O$, 99 %, Sigma-Aldrich), 2-methylimidazole (mIm; 99 %, Sigma-Aldrich), and polyethylene glycol ($PEG\text{-}_{400}$, average molecular weight = 400 $g.mol^{-1}$, Sigma-Aldrich) were used without further purification. Deionized water (resistivity > 18.2 MΩ) was obtained using a Barnstead Easy Pure II water purification system.

### Organic solvent-free synthesis of PEG-templated ZIF-8

Nanocrystalline ZIF-8 was synthesized in a purely aqueous system with the presence of $PEG\text{-}_{400}$ as both a solvent and a sacrificial template. The synthesis solution was prepared as follows: Firstly, 3.93 mmol (1.17 g) of $Zn(NO_3)_2\ 6.H_2O$ was dissolved in 10 g of deionized (DI) water and 5 ml $PEG\text{-}_{400}$. Secondly, 63.94 mmol (5.25 g) of 2-methylimidazole was dissolved in a separate vessel with 35 g of DI water and 10 ml of $PEG\text{-}_{400}$. The 2-methylimidazole solution was subsequently added and mixed with the zinc nitrate solution under stirring at room temperature. The synthesis solution turned milky almost instantly after mixing of the solutions. After stirring

for 5 min, the product was separated by centrifugation (5000 rpm, 10 min) and then washed with DI water (5 × 40 ml). The obtained white powder was dried in a vacuum oven at 450 K for 24 h to yield the final product, PEG-templated ZIF-8 nanoparticles (ZIF-8 NPs).

**Characterization and identification**

The size and shape of the ZIF-8 crystals after drying were determined by transmission electron microscopy (TEM) using a Philips CM200 microscope. The particle size analysis was performed using image J software. Powder X-ray diffraction (PXRD) spectroscopy, thermogravimetric analysis (TGA), and Fourier transform infrared (FTIR) were performed using a Bruker D8 Discover Diffractometer, a Mettler Toledo STARe apparatus, and a Perkin Elmer Spectrum Two FTIR with the ATR accessory, respectively. Nitrogen adsorption isotherms were recorded using a Micromeritics ASAP 2420 apparatus to determine the pore volume and specific surface area of the samples. The isotherms were recorded in the relative pressure (P/P°) range of 0.005–0.99, where P° is the saturated vapor pressure of nitrogen at the liquid nitrogen (77 K). The adsorption of $N_2$ was considered as reaching equilibrium when the pressure was maintained at a constant value for 10 s. Prior to the measurement, the adsorbent sample was pretreated by evacuation under a reduced pressure of 2.7 Pa (20 mTorr) at 450 K for 24 h. The Brunauer-Emmett-Teller surface area, denoted $S_{BET}$, was calculated according to the criteria specified in the literature [114] by applying the corresponding models to the $0.05< P/P_0 <0.35$ range. The pore size distribution was determined using the Non-Local Density Functional Theory (NLDFT.

**Adsorption measurements**

Gas sorption experiments were conducted on an Autosorb-iQ-MP instrument from Quantachrome Instruments. The increase in volume at equilibrium was measured as a function of relative pressure. Sample weights were determined using a Sartorius BS-124S electrogravimetric balance with a sensitivity of 0.1 mg. For $N_2$ adsorption experiments at 77 K, a 50 mg sample of PEG-$_{400}$ templated ZIF-8 nanoparticles was analyzed after outgassing using a surface area analyzer from Quantachrome Instruments. For $CO_2$, $CH_4$, CO, and $N_2$ adsorption experiments at 273 K, 298 K, 323 K, and 353 K, respectively, approximately 1.0 g of sample was used. Prior to adsorption experiments, the samples underwent degassing at 450 K for 24 hours. $N_2$ adsorption isotherms at 77 K were measured with a liquid nitrogen bath. For $CO_2$, $CH_4$, CO, and $N_2$ adsorptions at 273 K, 298 K, 323 K, and 353 K, respectively, a water bath controlled by a refrigerated circulating bath (TF-HX-5A) from Shanghai Tian Feng Industrial Co., Ltd. was utilized. High-purity nitrogen ($N_2$, 99.999%) carbon dioxide ($CO_2$, 99.995%), and methane ($CH_4$,

99.994%) were obtained from Air Liquide, France. High-purity carbon monoxide (CO, 99.95%) and hydrogen ($H_2$, 99.999%) gases were purchased from Lind Gas, France.

## Highlights

- Well-defined ZIF-8 nanoparticles (< 50 nm) via rapid aqueous PEG-templated synthesis
- High $CO_2$ adsorption (1088 mg($CO_2$)/g at 298 K); superior vs. $CH_4$, CO, $N_2$ and $H_2$.
- Advanced insight into gas adsorption via multilayer model derived from statistical physics formalism.
- Steric and energetic parameters extracted for 5 gases; orientation and multilayers are different.
- Thermodynamic adsorption functions confirm exothermic and spontaneous adsorption.

## Author Contributions

Sana Ahmed Khalil: Conceptualization, Investigation, Writing–original draft. Nadhem Missaoui: Investigation, Visualization, review & editing, Writing-original draft, Project administration. Raedah A S Albalawi: Visualization, Formal analysis, Data curation. Ali A Keshk: Visualization, Validation, Conceptualization. Obaidallah Alatawi: Formal analysis, Software, Validation. Tahani A Albalawi: Investigation, Visualization, Validation, Data Curation. Andrew J Gross: Supervision, Conceptualization, Writing-review&; editing.


## Research Funding

This research has not received funding from any public, commercial, or non-profit agencies

## Acknowledgments

The authors extend their appreciation to the deanship of scientific research at University of Tabuk for funding this work through research group number (S-1443-0224).


## Conflict of interests

The authors declare that they have no known competing financial interests or personal relationships that could have appeared to influence the work reported in this paper.

## Data Availability Statement

The data that supports the findings of this study are available from the corresponding author upon reasonable request.


## Keywords:

$CO_2$ capture, gas adsorption, metal organic framework, microporous adsorbent, MOF, Zeolitic imidazolate framework, ZIF-8, statistical physics.


## References

[1] A. Hussain, *Sep. Sci. Technol.* **2012**, *47*, 1857–1865.

[2] T. Schneider, J. Teixeira, C. S. Bretherton, F. Brient, K. G. Pressel, C. Sch¨ar, A. P. Siebesma, *Nat. Clim. Change*. **2017**, *7*, 3–5.

[3] G. P. Peters, R. M. Andrew, J. G. Canadell, , S. Fuss, R. B. Jackson, J. I. Korsbakken, C. LeQuéré, N. Nakicenovic, *Nat. Clim. Chang.* **2017**, *7*, 118–122.

[4] B. Wang, X. Zhang, H. Huang, Z. Zhang, T. Yildirim, W. Zhou, S. Xiang, B. Chen, *Nano Res.* **2021**, *14*, 507–511.

[5] M. Cozier, *Gases Sci. Technol.* **2019**, *9*, 1084–1086.

[6] Q. Wang, J. Luo, Z. Zhong, A. Borgna, *Energy Environ. Sci.* **2011,** *4*, 42–55.

[7] D. Lozano-Castelló, J. Alcañiz-Monge, M. A. De La Casa-Lillo, D. Cazorla-Amorós, *Fuel*. **2002**, *81*, 1777–1803.

[8] M. Sevilla, R. Mokaya, *Energy. Environ. Sci*. **2014,** *7***,** 1250–1280.

[9] J. A. Turner, *Science*. **2004,** *305***,** 972-974.

[10] B. Metz, O. Davidson, H. C. De Coninck, M. Loos, & L. Meyer, *Cambridge: Cambridge University Press* **2005**.

[11] Y. Yin, Z. H. Wen, X. Q. Liu, L. Shi, &, A. H. Yuan, *J. Porous. Mater*. **2018**, *25*, 1513-1519.

[12] R. Xu, W. Pang, J. Yu, Q. Huo, J. Chen, *John Wiley & Sons*. **2009**.

[13] R. T. Yang, Butterworth, *Boston*, **1987**.

[14] J. R. Li, R. J. Kuppler, H. C. Zhou, *Chem. Soc. Rev*. **2009,** *38***,** 1477-1504.

[15] R. Sakwattanapong, A. Aroonwilas, A. Veawab, *Ind. Eng. Chem. Res.* **2005**, *44*, 4465–4473.

[16] L. F. Ding, A. O. Yazaydin, *Phys. Chem. Chem. Phys.* **2013,** *15*, 11856–11861.

[17] A. Chakma, A. Meisen, *Ind. Eng. Chem. Prod. Res. Dev.* **1986**, *25*, 627–630.

[18] Y. D. Tang, K. Landskron, *J. Phys. Chem. C.* **2010**, *114*, 2494–2498.

[19] M. Pera-Titus, *Chem. Rev.* **2014**, *114*, 1413–1492.

[20] J. Y. Lee, C. D. Wood, D. Bradshaw, M. J. Rosseinsky, *A.I. Cooper, Chem. Commun.* **2006**, *25*, 2670–2672.

[21] R. V. Siriwardane, M. S. Shen, E. P. Fisher, *J. Losch, Energy Fuels*, **2005**, 19, 1153–1159.

[22] Zhu, W., Chen, M., Jang, J., Han, M., Moon, Y., Kim, J., Kim, J.. *Carbohydrate Polymers*, **2024**, *323*, 121393.

[23] M. Mansour, M. Guergueb, N. Missaoui, C. Castillo, E. Guitierrez Puebla, B. Ayed, H. Kahri, *ChemistrySelect*, **2024**, *15*, e202400487.

[24] F. A. Aloufi, N. Missaoui, R. F. Halawani, H. Kahri, B. Jamoussi, A. J. Gross, *Environ. Sci. & Pollut. Res.* **2024,** 1-18.

[25] H. R. Abid, G. H. Pham, H. M. Ang, M. O. Tade, S. Wang, *J. Colloid. Interface Sci.* **2012,** *366*, 120-124.

[26] Z. Bao, L. Yu, Q. Ren, X. Lu, S. Deng, *J. Colloid Interface Sci.* **2011**, *353*, 549–556.

[27] H. Zhang, X.L. Lv, G. M. Wang, J. R. Li, *J. Am. Chem. Soc*, **2012,** *134*, 10055-10058.

[28] Q. Wang, J. A. Johnson, D. H. Olson, D. G. Truhlar, *J. Am. Chem. Soc.* **2012**, *134*, 2169-2183.

[29] N. Missaoui, A. Chrouda, H. Kahri, A. J. Gross, M. R. Ardani, P. A. Ling, M. Ahmadipour, *Sep. Purif. Technol.* **2023**, *316*, 123755.

[30] Y. K. Tian, Y. M. Zhao, Z. X. Chen, G. N. Zhang, L. H. Weng, D. Y. Zhao, *Chem. Eur. J.* **2007**, *13*, 4146–4154.

[31] T. Wu, X. Bu, R. Liu, Z. Lin, J. Zhang, P. Feng, *Chem. Eur. J.* **2008**, *14*, 7771–7773.

[32] K.S. Park, Z. Ni, A.P. Coˆte´, J.Y. Choi, R. Huang, F.J. Uribe-Romo, H.K. Chae, M. O'Keeffe, O.M. Proc. *Natl. Acad. Sci* . **2006**, *103*, 10186–10191.

[33] B. Wang, A. P. Coˆte´, H. Furukawa, M. O'Keeffe, O. M. Yaghi, *Nature*. **2008**, *453*, 207–211.

[34] W. Morris, N. He, K. G. Ray, P. Klonowski, H. Furukawa, I.N. Daniels, Y. A. Houndonougbo, M. Asta, O.M. Yaghi, B. B. Laird, *J. Phys. Chem.* **2012**, *116*, 24084–24090.

[35] D. Danaci, R. Singh, P. Xiao, P.A. Webley, *Chem. Eng. J.* **2015**, *280*, 486–493.

[36] J. Ethiraj, S. Palla, H. Reinsch, *Microporous. Mesoporous.Mater.* **2020**, *294*, 109867.

[37] J. McEwen, J.D. Hayman, A.O. Yazaydin, *Chem. Phys*. **2013**, *412*, 72-76.

[38] N. Missaoui, H. Kahri, U. B. Demirci, *J. Mater. Sci*. **2022**, *57*, 16245-16257.

[39] B. Assfour, S. Leoni, G. Seifert, *J. Phys. Chem. C.* **2010**, *114*, 13381-13384.

[40] Y. Wang, Z. Lan, X. Huang, H. Liu, j. Guo, *Int. J. Hydrog. Energy*. **2019**, *44*, 28863-28873.

[41] J. Hwang, H. Azzan, R. Pini, C. Petit, *J. Chem. Eng. Data*. **2022**, *67*, 674-1686.

[42] Y. R. Lee, M. S. Jang, H. Y. Cho, H. J. Kwon, S. Kim, W. S. Ahn, *J. Chem. Eng*. **2015**, *271*, 276–280.

[43] J. Gordon, H. Kazemian, S. Rohani, *Microporous. Mesoporous. Mater.* **2012**, *162*, 36–43.

[44] F. Wang, H. Guo, Y. Chai, Y. Li and C. Liu, *Microporous. Mesoporous. Mater.* **2013**, *173*, 181–188.

[45] S. Diring, S. Furukawa, Y. Takashima, T. Tsuruoka and S. Kitagawa, *Chem. Mater*. **2010**, *22*, 4531–4538.

[46] K. M. Taylor, A. Jin, W. Lin, Angew. *Chem. Int. Ed*. **2008**, *47*, 7722–7725.

[47] T. Xing, Y. Lou, Q. Bao, J. Chen, *Cryst. Eng. Comm*. **2014**, *16*, 8994-9000.

[48] M. Zhao, K. Yuan, J. Wang, J. Zhou, *Chem. comm*. **2011**, *47*, 1601-1603.

[49] R. Banerjee, A. Phan, B. Wang, C. Knobler, H. Furukawa, M. O'Keeffe, O. M. Yaghi, *Science*. **2008**, *319*, 939-943.

[50] A. Alowasheeir, N. L. Torad, T. Asahi, S. M. Alshehri, T. Ahamad,, Y. Bando, M. Han, *Sci Technol. Adv. Mat.* **2024**, *1*, 2292485.

[51] S. Ma, X. S. Wang, C. D. Collier, E. S. Manis, H. C. Zhou, *Inorg. Chem.* **2007**, *46*, 8499-8501.

[52] S. Qadir, Y. Gu, S. Ali, D. Li, S. Zhao, S. Wang, *Chem. Eng. J.* **2022,** *428*, 131-136.

[53] Z. Zhang, Q. Ding, S.B. Peh, D. Zhao, J. Cui, X. Cui, H. Xing, *ChemComm.* **2020,** *56*, 7726-7729.

[54] Y. Shi, Y. Xie, H.Cui, A. Z. Alothman, O. Alduhaish, R. B. Lin, B. Chen, *Chem. Eng. J.* **2022**, *446*, 137101.

[55] X. Wu, B. Yuan, Z. Bao, S. Deng, *J. Colloid. Interface. Sci.* **2014**, *430*, 78-84.

[56] H. Zhang, X.L. Lv, G.M. Wang, J.R. Li, *J. Am. Chem. Soc.* **2012**, *134*, 10055-10058.

[57] M. Thommes, K. Kaneko, A. V. Neimark, J. P. Olivier, F. Rodriguez-Reinoso, J. Rouquerol, &, K. S. Sing, *Pure. Appl. Chem*. **2015**, *87*, 1051-1069.

[58] Q. Chen, L. Hong, S. K. Jiang, C. X. Zhang, S. Li. Wang, W. X, M. L. Liu, *J. Membr. Sci.* **2023**, *675*, 121520.

[59] H. Wang, T. Li, J. Li, W. Tong, &, C. Gao, *Colloids Surf. A: Physicochem. Eng. Asp.* **2019**, *568*, 224-230.

[60] D. Feng, Z. Y. Gu, J. R. Li, H. L. Jiang, Z. Wei, H. C. Zhou, Angew. *Chem., Int. Ed.* **2012**, *51*, 10307-10310.

[61] K. Li, M. Chen, L. Chen, S. Zhao, W. Pan, P. Li, Y. Han, *Environ. Res.* **2024**, *241*, 117588.

[62], M. S. Christian, M. J. Hurlock, T. M. Nenoff, &, J. M. Rimsza, *J. Mol. Liq.***2024**, *395*, 123913.

[63] A. Chaouiki, M. Chafiq, &, Y. G. Ko, *Environ. Res.* **2024**, *246*, 118112.

[64] S. Oh, S. Lee, G. Lee, &, M. Oh, *Scientific Reports.* **2023**, *13*, 12250.

[65] X. Bi, X. Liu, L. Luo, S. Liu, Y. He, L. Zhang, &, T. You, *Inorg. Chem.* **2024**, *63* 2224-2233.

[66] Z. Li, B. He, &, S. Tang, *CrystEngComm.* **2024**, *26*, 70-79.

[67] S. K. Nune, P. K. Thallapally, A. Dohnalkova, C. Wang, J. Liu, G.J. Exarhos, *Chem. Comm*. **2010**, *46*, 4878–4880.

[68] Y. Yue, Z.-A.Qiao, X. Li, A. J. Binder, E. Formo, Z. Pan, C. Tian, Z. Bi and S. Dai, *Cryst. Growth. Des.* **2013,** *13*, 1002–1005.

[69] K. M. Koczkur, S. Mourdikoudis, L. Polavarapu, S. E. Skrabalak, *Dalton.Trans.* **2015**, *44*, 17883-17905.

[70] D. Kim, J. Park, J. Park, J. Jang, M. Han, S. H. Lim, J. Kim, *Small Methods*, **2024**, 2400236.

[71] J. Pérez-Pellitero, H. Amrouche, F.R. Siperstein, G. Pirngruber, C. Nieto-Draghi, G. Chaplais, A. Simon-Masseron, D. Bazer- Bachi, D. Peralta, N. Bats, *Chem. Eur. J.* **2010**, *16*, 1560–1571.

[72] C. Chen, J. Kim, D.A. Yang, W.S. Ahn, *J. Chem. Eng.* **2011**, *168*, 1134–1139.

[73] R. Bose, J. Ethiraj, P. Sridhar, J.J. Varghese, N.S. Kaisare, P. Selvam, *Adsorption.* **2020**, *26*, 1027–1038.

[74] N. Missaoui, M. Bouzid, A. Chrouda, H. Kahri, H. Barhoumi, A.L. Pang, M. Ahmadipour, *Microporous. Mesoporous. Mater*. **2023**, *360*, 112711.

[75] A. G. Castro, J. E. de Oliveira, E. Reguera, E. Vilarrasa-García, E. Rodríguez-Castellón, C.L. Cavalcante Jr, *Biol. Chem. Res.* **2017,** 234-246.

[76] C. H. Belgacem, N. Missaoui, M. A. H. Khalafalla, G. Bouzid, H. Kahri, A. H. Bashal, Y. Zhou, *J. Environ. Chem. Eng.* **2024**, *12*, 112086.

[77] M. Songolzadeh, M. Soleimani, M. T. Ravanchi, R. Songolzadeh, *The Scientific World Journal.* **2014**, *2014*, 828131-828165.

[78] J. Wang, Y. Wang, Y. Zhang, A. Uliana, J. Zhu, J. Liu, B. Van der Bruggen, *ACS. Appl. Mater Interfaces.* **2016,** *8*, 25508–25519.

[79] J. J. Beh, J. K. Lim, E. P. Ng, &, B. S. Ooi, *Mater. Chem. Phy*. **2018**, *216*, 393-401.

[80] Y. Pan, D. Heryadi, F. Zhou, L. Zhao, G. Lestari, H. Su, &, Z. Lai, *CrystEngComm*. *13* **2011**, *13*, 6937-6940.

[81] J. Cousin Saint Remi, T. Rémy, V. Van Hunskerken, S. van de Perre, T. Duerinck, M. Maes, D. De Vos, E. Gobechiya, C. E. Kirschhock, G. V. Baron, J. F. Denayer, *Chem. Sus. Chem.* **2011**, *4*, 1074-1077.

[82] E. L. Bustamante, J. L. Fernández, J. M, Zamaro, *J. Colloid. Interface. Sci.* **2014**, *424*, 37–43.

[83] J. Cravillon, S. Mu¨nzer, S. J. Lohmeier, A. Feldhoff, K. Huber, M. Wiebcke, *Chem. Mater.* **2009**, *28*, 1410–1412.

[84] M. J. Ordonez, K. J. Jr. Balkus, J.P. Ferraris, I. H. Musselman, *J. Membr. Sci.* **2010**, *361*, 28–37.

[85] A. Jomekian, R. M. Behbahani, T. Mohammadi, A. Kargari, *Microporous. Mesoporous. Mater.* **2016,** *234*, 43–54.

[86] Y. Guan, J. Shi, M. Xia, J. Zhang, Z. Pang, A. Marchetti, X. Wang, J. Cai, X. Kong, *Appl. Surf. Sci.* **2017**, *423*, 349–353.

[87] S. A. Ayon, M. M. Billah, S. S. Nishat, A. Kabir, *J. Alloys. Compd.* **2021**, *856*, 158217.

[88] Y. Pan, Y. Liu, G. Zeng, L. Zhao, Z. Lai, *Chem. Comm.* **2021**, *47*, 2071–2073.

[89] J. Yan, B. Zhang, Z. Wang, *Polym. Chem.* **2016,** *7*, 7295-7303.

[90] J. A. Mason, K. Sumida, Z. R. Herm, R. Krishna, J. R. Long, *Energy. Environ. Sci.* **2011,** *4*, 3030–3040.

[91] G. Ortiz, S. Brandès, Y. Rousselin, R. Guilard, *Chem. Eur. J.* **2011**, *17*, 6689-6695.

[92] Z. Zhang, Z. Li, and J. Li, *Langmuir*. **2012**, *28*, 12122-12133.

[93] P. Chowdhury, C. Bikkina, S. Gumma, *J. Phys. Chem. C.* **2009**, *113*, 6616–6621.

[94] M. Bouzid, N. Bouaziz, Y. B. Torkia, A. B. Lamine, *J. Mol. Liq*. **2019**, *283*, 674-687.

[95] A. Nakbi, M. Bouzid, F. Ayachi, F. Aouaini, A. B. Lamine, *Prog. Biophys. Mol. Biol.* **2019**, *149*, 70-85.

[96] A. Nakbi, M. Bouzid, F. Ayachi, N. Bouaziz, A. B. Lamine, *J. Mol. Liq*. **2020**, *298*, 111950.

[97] A. B. Lamine, Y. Bouazra, *Chem. Senses.* **1997**, *22*, 67- 75.

[98] M. Bouzid, Q. Zhu, G. D. Moggridge, A. B. Lamine, *J. Mol. Liq.* **2018**, *263*, 41-421.

[99] B. Diu, C. Guthmann, physique statistique, Hermann, *Paris*. **1989,** 676- 687.

[100] M. Bouzid, L. Sellaoui, M. Khalfaoui, H. Belmabrouk, A. B. Lamine, *Phys. A: Stat. Mech. Appl*. **2016**, *444*, 853-869.

[101] X. Pang, M. Bouzid, J. M. N. dos Santos, M. H. Gazzah, M. G. L. Dotto, H. Belmabrouk, A. Bajahzard A. Ertoe, Z. Li, *Colloids. Surf. A: Physicochem. Eng. Asp*. **2020**, *589*, 124467.

[102] W. Sghaier, Y. B. Torkia, M. Bouzid, A. B. Lamine, *J. Environ. Chem. Eng*. **2021**, *9*, 105108.

[103] S. Wjihi, L. Sellaoui, M. Bouzid, H. Dhaou, S. Knani, A. Jemni, A. B. Lamine, *Int. J. Hydrog. Energy*, **2017**, *42*, 2699-2712.

[104] Y. B. Torkia, M. Atrous, M. Bouzid, M. G. L. Dotto, A. B. Lamine, *Chem. Eng. Commun.* **2020**, *207*, 445-457.

[105] I. B. Khemis, K. Oueslati, M. Bouzid, N. Mechi, S. Wjihi, A. B. Lamine, J. *Mol. Liq.* **2021**, *322*, 114553.

[106] Y. B. Torkia, W. Sghaier, M. Bouzid, M. Trabelsi, A. B. Lamine, *Sep. Sci. Technol*. **2021**, *56*, 2578-2586.

[107] A. Bajahzar, M. Bouzid, C. Briki, F. Nasri, H. Belmabrouk, A. Jemni, *Int. J. Hydrog. Energy.* **2020**, *45*, 15281-15293.

[108] N. B. H. Mohamed, S. Ouni, M. Bouzid, M. Bouzidi, A.B. Petriciolet, M. Haouari, *Environ. Sci. Pollut. Res.* **2022** 1-17.

[109] W. Sghaier, Y. B. Torkia, M. Bouzid, A. B. Lamine, *J. Int. Acad. Refrig.* **2022**, *141*,119-131.

[110] N. Bouaziz, M. B. Manaa, M. Bouzid, A. B. Lamine, *Mol. Phys.* **2020**, *118*, e1606460.

[111] M. Bouzid, F. Nasri, H. Belmabrouk, *Sens. Lett.* **2016**, *14*, 1079-1083.

[112] F. Aouaini, S. Bouzgarou, M. Bouzid, S. Nasr, D. Choukaier, A. B. Lamine, *Sep. Sci. Technol.* **2022**, *57*, 2532-2542.

[113] M. Atrous,Y. B. Torkia, T. Selmi, M. Bouzid, M. Seffen, A. B. Lamine, *Chem. Pap*. **2022**, *76*, 4333–4339.

[114] J. Wannassi, N. Missaoui, C. Mabrouk, H. Barhoumi, R. D. Crapnell, N. Jaffrezic-Renault, C. E. Banks, H. Kahri, *J. ELECTROCHEM. SOC.* **2023**, *170*, 117504.